Monthly Notices of the ROYAL ASTRONOMICAL SOCIETY

MNRAS **490,** 5103–5121 (2019) doi:10.1093/mnras/stz2856
Advance Access publication 2019 October 12

Using HARPS-N to characterize the long-period planets in the PH-2 and Kepler-103 systems

Sophie C. Dubber,[1,2]★ Annelies Mortier,[2,3] Ken Rice,[1,4] Chantanelle Nava,[5] Luca Malavolta,[6] Helen Giles,[7] Adrien Coffinet,[7] David Charbonneau,[5] Andrew Vanderburg,[8]† Aldo S. Bonomo,[9] Walter Boschin,[10,11,12] Lars A. Buchhave,[13] Andrew Collier Cameron,[2] Rosario Cosentino,[10] Xavier Dumusque,[7] Adriano Ghedina,[10] Avet Harutyunyan,[10] Raphaëlle D. Haywood,[5]† David Latham,[5] Mercedes López-Morales,[5] Giusi Micela,[14] Emilio Molinari,[15] Francesco A. Pepe,[7] David Phillips,[5] Giampaolo Piotto,[16] Ennio Poretti,[10,17] Dimitar Sasselov,[5] Alessandro Sozzetti[9] and Stéphane Udry[7]

Affiliations are listed at the end of the paper

Accepted 2019 October 7. Received 2019 October 3; in original form 2019 August 1

ABSTRACT

We present confirmation of the planetary nature of PH-2b, as well as the first mass estimates for the two planets in the Kepler-103 system. PH-2b and Kepler-103c are both long-period and transiting, a sparsely populated category of exoplanets. We use *Kepler* light-curve data to estimate a radius, and then use HARPS-N radial velocities to determine the semi-amplitude of the stellar reflex motion and, hence, the planet mass. For PH-2b we recover a 3.5σ mass estimate of $M_{\rm p} = 109^{+30}_{-32}$ $\rm M_\oplus$ and a radius of $R_{\rm p} = 9.49 \pm 0.16$ $\rm R_\oplus$. This means that PH-2b has a Saturn-like bulk density and is the only planet of this type with an orbital period $P > 200$ d that orbits a single star. We find that Kepler-103b has a mass of $M_{\rm p,b} = 11.7^{+4.31}_{-4.72}$ $\rm M_\oplus$ and Kepler-103c has a mass of $M_{\rm p,c} = 58.5^{+11.2}_{-11.4}$ $\rm M_\oplus$. These are 2.5σ and 5σ results, respectively. With radii of $R_{\rm p,b} = 3.49^{+0.06}_{-0.05}$ $\rm R_\oplus$ and $R_{\rm p,c} = 5.45^{+0.18}_{-0.17}$ $\rm R_\oplus$, these results suggest that Kepler-103b has a Neptune-like density, while Kepler-103c is one of the highest density planets with a period $P > 100$ d. By providing high-precision estimates for the masses of the long-period, intermediate-mass planets PH-2b and Kepler-103c, we increase the sample of long-period planets with known masses and radii, which will improve our understanding of the mass–radius relation across the full range of exoplanet masses and radii.

Key words: techniques: photometric – techniques: radial velocities – techniques: spectroscopic – planets and satellites: composition.

1 INTRODUCTION

The photometric transit method, which allows for an estimate of a planet's radius (e.g. Charbonneau et al. 2000; Batalha et al. 2011), and the radial velocity (RV) method, which allows for an estimate of a planet's mass (e.g. Vogt et al. 2010; Bonfils et al. 2011), can be combined to infer a planet's internal composition and determine if it still retains a volatile envelope (e.g. Rogers 2015). Ideally, we would like a large sample of exoplanets, ranging from small, rocky planets up to large gas giants, with a wide range of orbital periods and precise mass and radius estimates, so that we can develop a good understanding of the potential underlying mass–radius (MR) relation.

The advent of NASA's *Kepler* spacecraft has significantly increased the sample of exoplanets with precise radius estimates. Highly precise radial velocity spectrometers, such as HARPS (Mayor et al. 2003) and HARPS-N (Cosentino et al. 2012), have also allowed for follow-up observations to determine precise mass estimates, especially for small planets. For example, a specific goal of the HARPS-N collaboration has been to follow up and provide precise mass estimates for some of the small exoplanets discovered by *Kepler* and *K2*. Examples include Kepler-93b (Dressing et al.

★ E-mail: dubber@roe.ac.uk
† NASA Sagan Fellow.

2015), Kepler-21b (López-Morales et al. 2016), and K2-263b (Mortier et al. 2018).

Of particular current interest is the detection of a gap in the radius distribution for lower-mass planets (Fulton et al. 2017). It appears that planets either have radii less than $\sim$1.5 $R_\oplus$ and are pre-dominantly rocky or have radii above $\sim$2 $R_\oplus$ and still retain a substantial volatile atmosphere. Although the origin of this gap is not clear, the existence of such a gap was predicted (Owen & Wu 2013; Lopez & Fortney 2014) for close-in planets subject to high levels of irradiation. The population of close-in, low-mass exoplanets appears consistent with this photoevaporation scenario (e.g. Van Eylen et al. 2018; Rice et al. 2019).

This does mean that less attention has been paid to slightly larger planets, of intermediate mass, that may help us to better understand the overall relation between planet mass and radius. Obtaining highly precise mass measurements can require committing a lot of time to the observations. The number of observations required scales as $N \propto (\sigma/K)^2$, where σ is the precision of a single RV measurement and K is RV semi-amplitude (Gaudi & Winn 2007). Clearly, the number of observations needed to obtain a highly precise mass can vary for each target and set of observing conditions, but in general for a given error level, more measurements are required for a planet of a lower mass. This focus on low-mass planets means that we have spent less time observing those systems with known planets that are probably of intermediate mass.

There is also a scarcity of long-period planets (here defined as $P > 100$ d) with both masses and radii precisely determined. This is primarily due to the low probability of observing the transit of such a planet, which scales inversely with the orbital period (Beatty & Gaudi 2008). This gap in the population is thus a result of observational biases, rather than a real feature of the distribution of exoplanets. Radial velocity observations of long-period, transiting planets are also rare, since longer observation times are needed to cover enough of an orbit to constrain the radial velocity curve. Despite the observational challenges, planets in this part of the parameter space deserve to be extensively studied, which will also remove the manifestation of observational biases from our understanding of the population. Currently, only a handful of long-period planets are well characterized: examples include HD80606b (Naef et al. 2001; Moutou et al. 2009), characterized by extensive RV monitoring, and Kepler-51 (Ford et al. 2011; Hadden & Lithwick 2017), characterized by transit timing variations (TTVs). This population of giant planets is a key tool in testing predictions of internal structure and evolution of giant planets. For example, their increased orbital distance means they ought to be significantly less inflated than their closer-in siblings. Furthermore, these detections are crucial for filling out the period-density parameter space: Direct imaging observations regularly detect very long-period planets, but determining a density for these objects is challenging.

There have been a number of attempts to develop an MR relation, which would increase the number of exoplanets with density estimates. Seager et al. (2007) suggested a power-law function for solid exoplanets, allowing the slope to change depending on the mass range. They used simplified equations of state for iron cores and silicate- or water-dominated mantles. Lissauer et al. (2011) fitted a relation to mass and radius data for Solar system planets, but recognized that this simpler approach was insufficient when considering large planets. However, a unique MR relation may not exist at all (see Ning, Wolfgang & Ghosh 2018, for an overview). In 2014, Weiss & Marcy used a larger sample of 65 Earth-to-Neptune-sized exoplanets and found that a simple power-law fit had a large scatter in mass for a given radius, due to different compositions. More recently, Wolfgang, Rogers & Ford (2016) first quantified how this intrinsic scatter varies as a function of radius. Chen & Kipping (2017) developed a predictive model using a probabilistic MR relation that spans a larger parameter space than previous works and also treats the transition points between different planet populations as inferred parameters. They demonstrate the need for different power laws for the different populations, with clear transitions between each.

The current data set is still too limited to prove the existence of an MR relation definitively. Thus, it has become increasingly important to use all available observational data to increase the sample of planets with known masses, including those where the result may be less precise than we would like. Typically, detection papers focus on $>6\sigma$ results for planet masses (e.g. Haywood et al. 2018; Malavolta et al. 2018), and even higher precision for radii. Requiring this level of precision for detections places severe practical limits on the number of planets for which well-constrained masses and radii are available. However, detections of lower significance can still add useful data points to the sample of known planets, as long as well-constrained posterior mass distributions are produced.

When HARPS-N was initially commissioned, one of the priorities of the Science Team was to perform follow-up investigations of objects identified by the *Kepler* survey (Borucki et al. 2010). Subsequently this became follow-up for the K2 survey and it has been further extended by the launch of the *Transiting Exoplanet Survey Satellite* (*TESS*) (Ricker et al. 2015), for which HARPS-N will also aim to carry out follow-up observations. Objects observed in the K2 survey were generally brighter targets, meaning that some of the *Kepler* objects initially observed by HARPS-N were later classed as lower priority. Even the best techniques at the time were unable to observe any clear planetary signals. However, the progression of analysis techniques in the six years since the beginning of HARPS-N observations now means that these lower-priority targets may in fact still be conducive to well-constrained results. We chose to revisit some of these targets, to check that good data were not being wasted, and also to potentially increase the sample of exoplanets in a region of parameter space that is currently not well populated. We found that with the improved techniques, such as Gaussian process (GP) regression modelling (Haywood et al. 2014), we were indeed able to use this revisited data to find, in some cases, well-constrained planetary masses.

Here, we revisit two HARPS-N targets, PH-2 and Kepler-103 (see Table 1 for stellar parameters), identified as planetary candidates by the *Kepler* survey (Borucki et al. 2010). Both PH-2 and Kepler-103 are solar-type stars, with G3 and G2 spectral types and visual magnitudes of $V = 12.70$ and $V = 12.36$, respectively (Henden et al. 2015). We performed multiple follow-up RV observations using HARPS-N aiming to confirm the planetary nature of the candidates and to provide mass estimates. We report a 3.5σ RV semi-amplitude value for the Saturn-like, long-period planet PH-2b (also known as Kepler-86b). This planet was first identified as a planetary candidate (KOI-3663b) by Wang et al. (2013). We were also able to constrain the masses of the two planets in the Kepler-103 system (KOI-108), presenting a 2.5σ result for Kepler-103b and a 5σ result for Kepler-103c. Both Kepler-103b and Kepler-103c have previously published mass constraints (Marcy et al. 2014), but neither of the masses was precisely measured in this earlier work. We find Kepler-103b to be a super-Earth on a relatively close-in orbit, whereas Kepler-103c is a wide-orbit, high-density giant planet.

We present the *Kepler* and HARPS-N observations for each of the systems in Section 2. We discuss the stellar analysis in Section 3. The transit and RV analysis are described in Sections 4

Table 1. Stellar parameters for each of the target stars. We show the 2MASS *J*, *H*, and *K* magnitudes, taken from Skrutskie et al. (2006), *V* magnitudes from APASS DR9 (Henden et al. 2015), values of $T_{\rm eff}$, [Fe/H], and log *g* determined using the FASMA EW method, and the *Gaia* parallaxes (Gaia Collaboration 2016, 2018). We also show the average value of $\log R'_{HK}$, determined from the HARPS-N spectra, the projected rotational velocity from Petigura et al. (2017), the $T_{\rm eff}$, [Fe/H], and log *g* values from the ISOCHRONES analysis (which agree well with those used as priors), and the resulting mass and radius values in solar units.

Parameter	Descriptor	PH-2	Kepler-103
J	2MASS *J* mag	11.501 ± 0.023	11.193 ± 0.021
H	2MASS *H* mag	11.182 ± 0.030	10.941 ± 0.016
K	2MASS *K* mag	11.116 ± 0.022	10.873 ± 0.017
V	APASS *V* mag	12.699 ± 0.010	12.360 ± 0.026
$T_{\rm eff}$ (K)	Effective temperature (FASMA)	5691 ± 67	6009 ± 64
[Fe/H]	Metallicity (FASMA)	−0.03 ± 0.04	0.16 ± 0.04
log *g* (cgs)	Surface gravity (FASMA)	4.42 ± 0.10	4.29 ± 0.10
π_{Gaia} (mas)	*Gaia* parallax	2.880 ± 0.030	1.992 ± 0.024
$T_{\rm eff}$ (K)	Effective temperature (ISOCHRONES)	5711^{+60}_{-59}	6047^{+50}_{-67}
[Fe/H]	Metallicity (ISOCHRONES)	−0.03 ± 0.04	0.15 ± 0.04
log *g* (cgs)	Surface gravity (ISOCHRONES)	4.45 ± 0.02	4.17 ± 0.02
M_* ($M_\odot$)	Stellar mass (ISOCHRONES)	0.958 ± 0.034	$1.212^{+0.024}_{-0.033}$
R_* ($R_\odot$)	Stellar radius (ISOCHRONES)	$0.961^{+0.016}_{-0.015}$	$1.492^{+0.024}_{-0.022}$
$v \sin i$ (km s^{-1})	Projected rotational velocity	2.0 ± 1.0	3.1 ± 1.0
$\log R'_{HK}$	Average value of the $\log R'_{HK}$ activity indicator	−4.848 ± 0.117	−5.069 ± 0.086

and 5, respectively. We discuss the results in Section 6, placing these measurements in the context of the existing field. Finally, we conclude in Section 7.

2 OBSERVATIONS

2.1 Kepler photometry

PH-2 was monitored with *Kepler* in long-cadence mode, observing every 29.4 min, in all quarters Q0–Q17, with transits only observed in Q4,Q7,Q10,Q13, and Q16. These observations cover a total time period of 1470 d (BJD 2454953.0375–2456423.500694).

Kepler-103 was also monitored in long-cadence mode in quarters Q0–Q17, covering the same time period. Transits were uncovered in every quarter of the data.

Long-term variations (on a *Kepler* quarter time-scale) are present in the simple aperture flux (SAP), as a result of differential velocity aberration. If this is not removed, it can obscure stellar rotation signals. We have chosen to work with the Presearch Data Conditioning SAP light curve from DR21 (Smith et al. 2012; Stumpe et al. 2012, 2014) as this version more effectively removes these trends (see Haywood et al. 2018 for further details).The full *Kepler* light curves for both stars are shown in Figs A1 and A2.

We followed a procedure similar to that of Haywood et al. (2018). In short, we fitted the PDCSAP short-cadence light curves produced by the *Kepler* pipeline (Smith et al. 2012; Stumpe et al. 2012). We flattened the light curve by fitting polynomials to the out-of-transit light curves near transits and dividing by the best-fitting polynomial. Depending on the number of points in the out-of-transit region near the transits, we chose either first order (linear) or second order (parabola) polynomials. We excluded outliers from the phase-folded light curve by dividing it into bins of a few minutes. These outliers are especially prevalent in time periods towards the end of the original *Kepler* mission, during which the second of four reaction wheels was close to failing. We then excluded any 3σ outliers that lie in each of these bins.

2.2 HARPS-N spectroscopy

To collect spectra of our targets, we used the high-resolution HARPS-N spectrograph ($R = 115\,000$) which is installed on the 3.6-m Telescopio Nazionale Galileo at the Observatorio del Roque de los Muchachos in La Palma, Spain (Cosentino et al. 2012, 2014). Observations were taken as part of the HARPS-N Collaboration's Guaranteed Time Observations programme. The spectra were used for both determining stellar parameters and obtaining high-precision radial velocities.

The spectra were reduced with version 3.9 of the HARPS-N Data Reduction Software (DRS), which includes corrections for colour systematics introduced by variations in seeing (Cosentino et al. 2012). The observed spectra were cross-correlated with a spectral template chosen to be the closest match to the spectral type of the target (Pepe et al. 2002). In this case, we used a G2 template for both objects. A Gaussian was fitted to the resulting cross-correlation function (CCF) so that the RV values and the associated errors could be determined. Other properties of the CCF can be used to ascertain activity indicators, such as the full width at half-maximum (FWHM), the contrast, and the bisector span (BIS). Additionally, the chromospheric indicator $\log R'_{\rm HK}$ was calculated from the Ca H&K lines (Noyes, Weiss & Vaughan 1984).

2.2.1 *PH-2 (Kepler-86)*

PH-2 was observed using HARPS-N in regular intervals between 2013 September 29 and 2016 May 19, to observe multiple orbits of the $P = 282$ d planet candidate. We collected 33 spectra, with typical exposure times of 1800 s (the exceptions being those taken on BJD = 2457164.71, 2457164.72, 2457165.70, 2457165.71, when the exposure times were 900 s due to exceptional weather conditions).

The majority of RV data points were obtained by observing with the second fibre on-sky. However, we eliminated one RV that was extracted from a spectrum observed with simultaneous thorium–argon rather than a simultaneous sky fibre (BJD = 2456573.50). Different templates used for observing can create an offset in RV

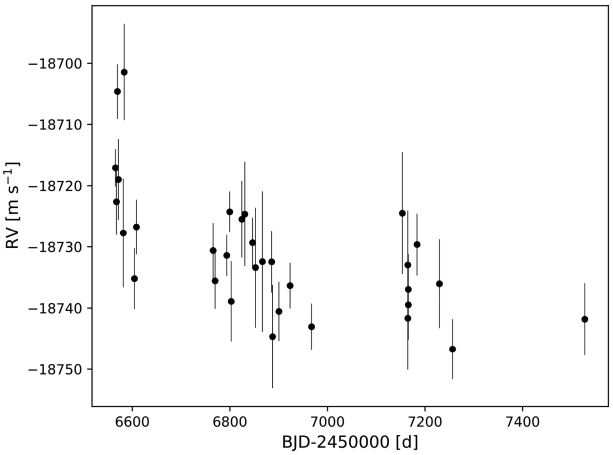

Figure 1. The HARPS-N RVs for PH-2, plotted against time.

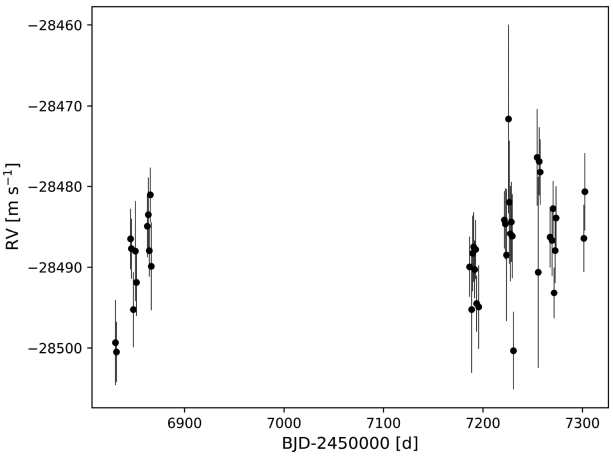

Figure 2. The HARPS-N RVs for Kepler-103, plotted against time.

measurements, and in this case the RV was significantly discrepant when including it in the data set. This led to a final data set of 32 RVs with signal-to-noise ratios in the range S/N = 13.7–38.9 at 550 nm (average S/N = 24.6). The average RV internal uncertainty was 6.1 m s^{-1}. The HARPS-N RVs for PH2 are shown in Fig. 1, and the RV data, associated 1σ errors, and activity indicators are shown in Table B1.

2.2.2 *Kepler-103 (KOI-108)*

We observed Kepler-103 regularly from 2014 May 22 until 2015 October 06. We then re-observed it starting on 2018 August 30 and ending on 2018 November 01. Our strategy was to take one observation per night with an exposure time of 1800 s (apart from observations on BJD = 2456865.56 and BJD = 2456866.51 when the exposure times were 1600 and 1500 s, respectively) and to observe the system for a few stellar rotation periods. This improved the window function and provided a sampling adequate to pick up potential signals due to stellar activity.

We collected a total of 60 RV spectra, with signal-to-noise ratios in the range S/N = 13.8–51.9 at 550 nm (average S/N = 31.1), and with an average RV internal uncertainty of 5.1 m s^{-1}.

The HARPS-N RVs for Kepler-103 are shown in Fig. 2 and the RV data, associated 1σ errors, and activity indicators are shown in Table C1.

3 STELLAR ANALYSIS

3.1 Atmospheric parameters

We used the high-resolution spectra from HARPS-N to determine the stellar atmospheric parameters. Using the estimated RVs, we shifted all spectra to the rest frame and then stacked the spectra, enhancing our signal to noise. Equivalent widths (EWs) were determined automatically using ARESv[1] (Sousa et al. 2015), using a line list of roughly 300 neutral and ionized iron lines taken from Sousa et al. (2011).

These EWs were then used as input to MOOG[2] (Sneden 1973) for line analysis to obtain effective temperatures, metallicity, and surface gravity, under the assumption of local thermodynamic equilibrium (LTE). This process was implemented using FASMA,[3] as described by Andreasen et al. (2017), and a correction was applied to the surface gravity in accordance with Mortier et al. (2014). Finally, we added systematic errors in quadrature, as outlined in Sousa et al. (2011), necessary to account for differences in values found using different methods. For the effective temperature, we added a systematic error of 60 K, for metallicity we added 0.04 dex, and for surface gravity we added 0.1 dex. The resulting parameter values for each star are given in Table 1.

As outlined in Borsato et al. (2019), using multiple methods to find different sets of stellar photospheric parameters is an important tool for getting realistic errors on the stellar mass and radius. Consequently, we also used CCFpams[4] to calculate an independent estimation of the same parameter values (Malavolta et al. 2017). The Mortier et al. (2014) surface gravity correction was again used. The parameter values are consistent with those determined using FASMA, with the exception of a 1σ difference in the metallicity of PH-2. Strong agreement of two independent methods gave us confidence that using only the FASMA results was sufficient for determining the stellar masses and radii.

3.2 Stellar mass and radius

The stellar mass and radius in each case were then found using the ISOCHRONES PYTHON package (Morton 2015). This uses both the Mesa Isochrones and Stellar Tracks (MIST; Dotter 2016) and the Dartmouth Stellar Evolution Database (Dotter et al. 2008). As priors we use the $T_{\rm eff}$, log g, and [Fe/H] values from the FASMA analysis, the 2MASS J, H, and K magnitudes (Skrutskie et al. 2006), and the *Gaia* parallax from Data Release 2 (Gaia Collaboration 2016, 2018). Using only the 2MASS J, H, and K magnitudes has been shown to be sufficient for estimating the masses and radii of stars of these spectral types (Mayo et al. 2018). We used both the MIST and Dartmouth model grids and posterior sampling was performed using MULTINEST (Feroz & Hobson 2008; Feroz, Hobson & Bridges 2009; Feroz et al. 2013).

The final estimate for each parameter is then determined by taking the 15.865th/84.135th percentiles of the combined posterior samples for all sets of stellar parameters. We recover a stellar mass and radius for PH-2 of $M_* = 0.958 \pm 0.034$ M$_\odot$ and $R_* = 0.961^{+0.016}_{-0.015}$ R$_\odot$. For Kepler-103, we find $M_* = 1.212^{+0.024}_{-0.033}$ M$_\odot$ and $R_* = 1.492^{+0.023}_{-0.022}$ R$_\odot$. Table 1 shows all the resulting parameters from the ISOCHRONES analysis. The output effective

[1]Available at http://www.astro.up.pt/ sousasag/ares/.
[2]Available at http://www.as.utexas.edu/ chris/moog.html.
[3]Available at http://www.iastro.pt/fasma/
[4]Available at https://github.com/LucaMalavolta/CCFpams

temperature, metallicity, and surface gravity all agree well with both of the methods used to initially estimate these parameters, implying that these results are independent of which method is chosen to supply the prior values.

3.3 Stellar activity

To assess the level of stellar activity, we looked at the autocorrelation functions (ACFs) of the *Kepler* light curves where we saw different degrees of significant variable structure. Therefore, it was only possible to make estimates of the stellar rotational periods, $P_{\rm rot}$, rather than determine both the rotational periods and activity lifetimes as described in Giles et al. (2017). Estimates for the stellar rotational period were extracted from the location of the first side lobe of the ACF, found through peak detection by means of a parabola fit. Our analysis recovered a rotation period of $P_{\rm rot} = 22.6$ d for PH-2 and $P_{\rm rot} = 20.8$ d for Kepler-103. Since no full fit of the ACF was performed, as in Giles et al. (2017), these are just rough estimates.

Additionally, we used the *Kepler* light curves to carry out a GP analysis using a quasi-periodic covariance kernel function (Haywood et al. 2014; Grunblatt, Howard & Haywood 2015; Angus et al. 2018). This combines a squared exponential and standard periodic kernel (Haywood et al. 2014) and allows us to most accurately include the effects of various stellar properties. The kernel is described by

$$\Sigma_{i,j} = h^2 \exp\left[-\frac{\sin^2[\pi(t_i - t_j)/\theta]}{2w^2} - \left(\frac{t_i - t_j}{\lambda}\right)^2\right], \quad (1)$$

where t_i and t_j are two times of observation and θ, w, h, λ are the 'hyperparameters'. These can be related to various stellar properties. For example, h (mag) is the amplitude of the correlated signal in the light curve caused by stellar activity, and θ (d) is equivalent to the rotational period of the star ($\theta = P_{\rm rot}$). The other two parameters are related to the evolution of the active regions on the surface of the star. λ (d) is the decay time-scale of the active regions, which is tied to their aperiodic variation, and w is the coherence scale, which is linked to the amount of active regions present at any time. The typical values of these parameters are known to varying degrees. Active-region decay times are of the order of weeks to months (Giles et al. 2017), and foreshortening and limb darkening restrict w to values of the order of 0.5, allowing no more than two to three peaks to develop in the light curve or RV curve per rotation cycle.

We used PYORBIT[5] (Malavolta et al. 2016), a package for modelling planetary and stellar activity signals (See Section 5.2). This implements the GP quasi-periodic kernel through the GEORGE package (Ambikasaran et al. 2015), optimizes the hyperparameters using the differential evolution code PYDE,[6] and then provides the optimized hyperparameters as starting values for the affine-invariant ensemble sampler EMCEE (Foreman-Mackey et al. 2013).

Since the GP regression typically scales with the third power of the number of data points, we could not use the full light curve. Instead, we used a sample of the light curve that would cover many rotation periods. For Kepler-103, we combined quarters 11, 12, and 13, while for PH-2 we combined quarters 15, 16, and 17. In both cases, we then removed the transits and any data points more than 5σ from the mean. We also binned the light curve every 10 data points and allowed for different offsets and jitters for each quarter.

[5]Available at https://github.com/LucaMalavolta/PyORBIT, version 8.
[6]Available at https://github.com/hpparvi/PyDE

Table 2. Results of the GP stellar activity analysis of the *Kepler* light-curve.

Parameter	PH-2	Kepler-103
$P_{\rm rot,ACF}$ (d)	22.6	20.8
$\theta = P_{\rm rot,GP}$ (d)	$17.16^{+6.14}_{-6.03}$	$21.45^{+1.15}_{-5.90}$
λ (d)	$6.29^{+5.96}_{-3.22}$	$11.42^{+2.51}_{-5.32}$
w	$0.286^{+0.225}_{-0.089}$	$0.242^{+0.102}_{-0.029}$
h (mag)$_-$	$0.00055^{+0.00005}_{-0.00004}$	$0.000085^{+0.000008}_{-0.000007}$

The results are presented in Table 2. The rotation periods recovered from the GP analysis are consistent with the results from the ACF analysis and plausible given their spectral type.

4 TRANSIT ANALYSIS

We performed transit fits to the photometric light-curve data of PH-2 and Kepler-103 using the publicly available MCMC software EXOFAST v2 (Eastman 2017). The global model used in EXOFAST v2 includes spectral energy density and integrated isochrone models to constrain stellar parameters. In the case of both targets, we set the */torres* flag in order to utilize stellar mass and radius relations published in Torres, Andersen & Giménez (2010). The default limb-darkening fit used by EXOFAST v2 is based on tables reported in Claret & Bloemen (2011). Relevant output parameters are listed in Tables 6 and 7 respectively, the resulting transit fits are shown in Fig. 3 for all three planets, and logistics of each fit are detailed below.

In the case of PH-2, we performed a fit using the five quarters of Kepler long-cadence light curves containing transits (Q4, Q7, Q10, Q13, Q16). We ran the MCMC fit for a maximum of 50 000 steps (*maxsteps* = 50 000), recording every twentieth step value as part of the final posterior distribution (*nthin* = 20). The default limb-darkening fit failed, so we set the *noclaret* flag to perform a solution ignoring the tables from Claret & Bloemen (2011). We performed a single-planet transit fit with open eccentricity, using the priors listed in Table 3. Priors on the two parameters related to the host star (effective temperature and metallicity) came from the analyses described in Section 3, while the prior on eccentricity came from the RV fit, and was required to break a degeneracy between stellar density and eccentricity.

In the case of Kepler-103, we fitted 18 quarters of long-cadence light curves (Q0–Q17), all containing transits. We ran the MCMC fit for a maximum of 5000 steps (i.e. *maxsteps* = 5000), recording every hundredth step value as part of the final posterior distribution (i.e. *nthin* = 100). We first performed a two-planet transit fit with both the planets fixed to circular orbits. In the first fit, we only applied priors on effective temperature, metallicity, and stellar radius, again provided by the analyses described in Section 3. The prior on stellar radius broke a degeneracy between R_* and the semi-amplitudes of the two planets in the system. The circular fit produced white residuals for transits of Kepler-103b; however, a signal near ingress and egress of Kepler-103c in the residuals suggested transit timing variations were present. We therefore performed a second fit keeping Kepler-103b fixed to a circular obit, but allowing for TTVs and an eccentric orbit in the fit to transits of Kepler-103c and using the priors listed in Table 3. In the second fit that allowed for TTVs and an eccentric orbit on the second planet, we also placed priors on orbital periods, central transit times, baseline flux, and the star-to-planet radius ratio for Kepler-103b, based on successful

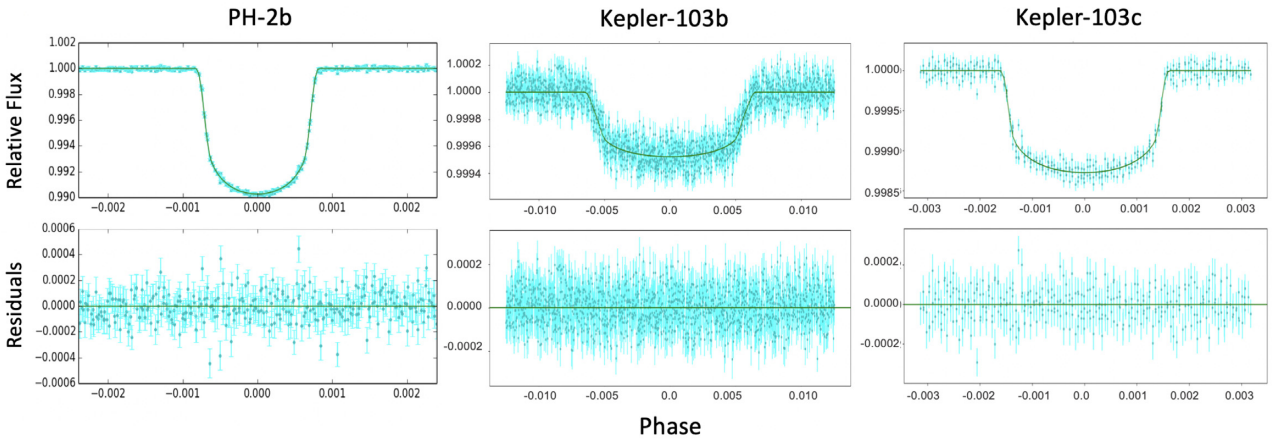

Figure 3. Phase-folded *Kepler* light curve for PH-2b, Kepler-103b, and Kepler-103c demonstrating the transits of the planet candidates in the systems.

Table 3. Parameters modelled in the EXOFAST v2 analysis and their prior probability distributions. See text for an explanation of the different prior parameters used for each system. Relevant final values are given in Tables 6 and 7.

ID	Parameter		Prior
PH-2	Eccentricity	e	Uniform (0.051 067, 0.155 592)
	Effective temperature	$T_{\rm eff}$	Gaussian (5961, 67)
	Metallicity	[Fe/H]	Gaussian (−0.03, 0.04)
Kepler-103	Orbital period	$P_{\rm b}$	(15.965 327 18, 0.000 012)
	’	$P_{\rm c}$	Gaussian (179.609 803, 0.0002)
	Central transit time	$T_{\rm C,b}$	Gaussian (844.652 46, 0.000 39)
	’	$T_{\rm C,c}$	Gaussian (834.159 77, 0.000 447)
	Radius ratio	$R_{\rm p,b}/R_*$	Gaussian (0.021 13, 0.000 20)
	Effective temperature	$T_{\rm eff}$	Gaussian (6009, 64)
	Metallicity	$[Fe/H]$	Gaussian (0.16, 0.04)
	Stellar radius	R_*	Gaussian (1.482, 0.021)
	Baseline flux	F_0	Gaussian (1.000, 0.001)

Table 4. Transit timing variations for the seven transits of the outer planet in the Kepler-103 system (Kepler-103c).

Transit No.	Transit Timing Variation (min)
1	$0.86^{+2.6}_{-2.4}$
2	$-11 + 4.3_{-4.5}$
3	$-23^{+3.2}_{-2.9}$
4	18 ± 2.4
5	10.2 ± 2.4
6	$7.6^{+3.0}_{-2.9}$
7	-34 ± 3.5

parts of our first circular fit. The central transit time in each case is given in the *Kepler* format, meaning $T_{\rm c,BJD} = T_{\rm c,KEP} + 2\,454\,833$. TTV results from our second fit to transits of Kepler-103c are listed in Table 4.

Relevant output parameters from these transit fits are given in Tables 6 and 7, along with the results from the radial velocity analysis for each system, discussed in the next section.

5 RADIAL VELOCITY ANALYSIS

5.1 Preliminary investigation

5.1.1 BGLS periodograms

To check for the presence of planetary signals, and to gain an initial understanding of the activity of each star, we carried out a Bayesian generalized Lomb–Scargle (BGLS) periodogram analysis (Mortier et al. 2015). The results are presented in Fig. 4, and show the period against the log of the power at each period.

In each case, we looked for signs of periodicity matching the rotation period of the star (indicated by the dashed line). This would be a sign of stellar activity in the RVs, and may indicate that activity should be included in the RV analysis. Due to the noise levels of the data, and thus the clarity of the BGLS, it is unclear as to whether this is the case for either target. PH-2 shows some power at the expected stellar rotation, but there is little indication of a periodic stellar activity signal in the Kepler-103 RVs.

The BGLS periodograms were also used to confirm the existence of the planetary signals, the periods of which are indicated by the solid black lines. The top panel shows a very clear signal at the period of PH-2b ($P = 282.5$ d), while the bottom panel shows a

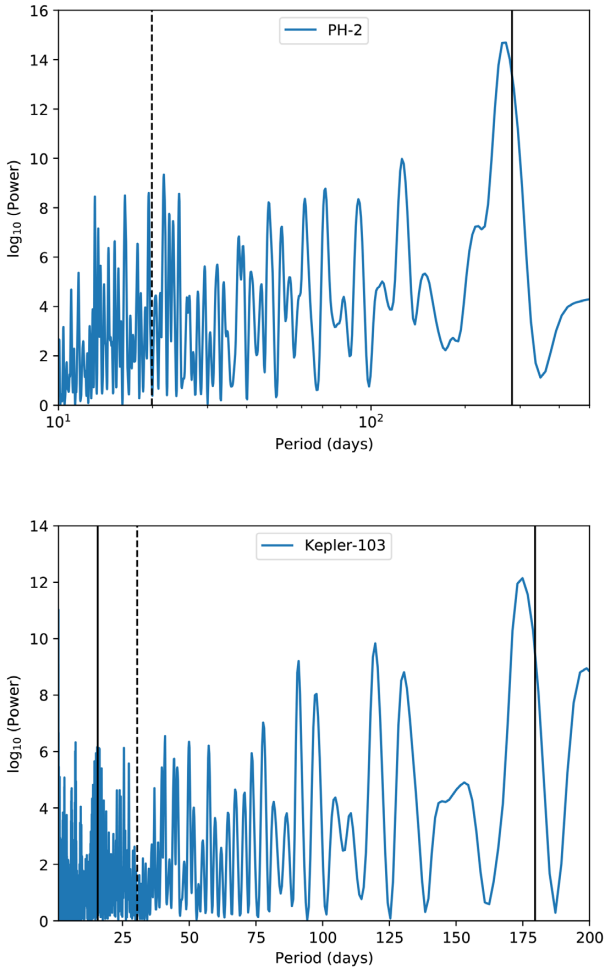

Figure 4. Bayesian generalised Lomb–Scargle periodograms of the RVs for PH-2 (top panel) and Kepler-103 (bottom panel). The solid lines indicate the expected periods of the known planets (PH-2b, Kepler-103b, and Kepler-103c). There are clear signals at the periods of PH-2b ($P \sim 282.5$ d) and Kepler-103c ($P \sim 179.6$ d). There is also an indication of a signal at the period of Kepler-103b ($P \sim 15.7$ d). The dashed lines indicate expected rotation periods of the star. There is some power at this period for PH-2, but little indication of a stellar rotation signal in the RVs of Kepler-103.

very clear signal at the period of Kepler-103c ($P = 179.6$ d). There is also an indication of a signal at the period of Kepler-103b ($P \sim 15.7$ d) in the bottom panel. This gave us confidence that we would be able to extract the radial velocity signatures of these planets.

5.1.2 Correlations

To further investigate the significance of the stellar activity, we looked at the correlations between the RVs and the activity indicators provided by the HARPS-N DRS (described in Section 2.2). If any showed a strong correlation, this could indicate that the RVs are strongly contaminated with signals relating to stellar activity.

The Pearson correlations coefficients, r, for correlations between RVs and four different activity indicators (BIS, contrast, FWHM, and $\log R'_{\rm HK}$), are shown in Table 5, for both PH-2 and Kepler-103. The r values given for the $\log R'_{\rm HK}$ were found using only non-zero values of this indicator. We consider any r values greater than ≈ 0.5 as showing signs of significant correlation. This is not the case for any of the indicators for PH-2 or Kepler-103, a sign that the RV data does not support including stellar activity terms in either fit. We note that the lack of correlations with these indices does not conclusively exclude the possibilty that stellar signals are present in the data (see e.g. Collier Cameron et al. 2019).

Table 5. Pearson correlation coefficients for correlations between RV and the different activity indicators for PH-2 and Kepler-103.

ID	$r_{\rm BIS}$	$r_{\rm Contrast}$	$r_{\rm FWHM}$	$r_{\log R'_{\rm HK}}$
PH-2	0.205	0.212	0.125	0.391
Kepler-103	0.165	0.117	0.153	0.019

5.2 Bayesian analysis

To carry out the RV analysis, and to extract planetary parameters from the RV data, we used PYORBIT (Malavolta et al. 2016). PYORBIT offers various options for the techniques used for each step of the analysis; here we used PYDE (Storn & Price 1997) for initial parameter determination and EMCEE (Foreman-Mackey et al. 2013) to do an MCMC parameter estimation. We used uniform priors for the radial velocity semi-amplitude, K, and for the eccentricity, e, and used Gaussian priors for the orbital period, P, and for the mid-transit time, $T_{\rm cent}$. The priors for the orbital period and mid-transit time are taken from the photometry analysis discussed in Section 4, as is the inclination, which is taken to be fixed.

The RV model fit is defined by

$$RV(t) = K\cos(\omega + \nu(t)) + Ke\cos(\omega) + \gamma. \quad (2)$$

Here, ν is the true anomaly, which is itself a function of t, e, P, and phase, ω is the argument of pericentre, and γ is the RV offset. Following the recommendations in Eastman, Gaudi & Agol (2013), we used $\sqrt{e}\sin\omega$ and $\sqrt{e}\cos\omega$ as fitting parameters rather than e and ω. The period and semi-amplitude are explored in logarithmic space. A jitter term $\sigma_{\rm jit}$ is also added in quadrature to the model errors to account for the white noise levels in the data.

5.2.1 PH-2

Wang et al. (2013) first reported the existence of a planet in the PH-2 system, discovered through the Planet Hunters project. Through false-probability analysis, they determined that the transit signal was caused by a giant planet at a 99.9 per cent confidence level. However, with only four RVs, they were unable to confirm this further. Our RVs and analysis here confirm the nature of the transit signal to be planetary.

The results of both the PYORBIT RV model and the EXOFAST transit model for PH-2 are shown in Table 6. The table shows the orbital period, P, and semi-major axis, a, in addition to the quantities derived from the RVs (radial velocity semi-amplitude, K, planet mass, $M_{\rm p}$, eccentricity, e, and mean density, ρ). We also give the uncorrelated jitter and the RV offset. The posterior distributions of the derived quantities are shown in Fig. D1. The expected lack of correlation between parameters is clearly visible, as is the convergence of the model to a final solution.

Fig. 5 shows the orbital solution and residuals from the PH-2 RV analysis. Our analysis recovers a RV semi-amplitude of $K = 11.47^{+3.01}_{-3.30}$ m s^{-1} and an eccentricity of $e = 0.28^{+0.12}_{-0.13}$. The errors on the final semi-amplitude (and thus mass) yield a better than 3σ result. Given the stellar mass of PH-2 and this RV semi-amplitude, we derive a mass for PH-2b of $M_{\rm p} = 108.81^{+29.79}_{-32.29}$ M$_\oplus$.

Table 6. Parameter values for PH-2b from the RV and transit analyses.

Parameter	Description	Value
Transit analysis		
P (d)	Orbital period	$282.525\,40^{+0.000\,10}_{-0.000\,11}$
$T_{\rm cent}$ (BJD)	Mid-transit time	$2\,455\,761.12272 \pm 0.000\,15$
$R_{\rm p}/R_*$	Radius ratio	$0.090\,39^{+0.000\,51}_{-0.000\,55}$
$R_{\rm p}$ ($R_\oplus$)[a]	Planet radius	9.49 ± 0.16
i (deg)	Inclination	$89.915^{+0.020}_{-0.022}$
a/R_*	Scaled semimajor axis	$185.76^{+3.89}_{-3.75}$
a (au)[a]	Orbital semimajor axis	$0.824^{+0.019}_{-0.017}$
RV analysis		
K (m s^{-1})	RV semi-amplitude	$11.47^{+3.01}_{-3.30}$
e	Eccentricity	$0.280^{+0.121}_{-0.133}$
ω	Argument of pericentre	$0.532^{+0.901}_{-0.796}$
$M_{\rm p}$ ($M_\oplus$)	Planet mass	$108.81^{+29.79}_{-32.29}$
$\rho_{\rm p}$ (g cm^{-3})	Planet density	$0.70^{+0.20}_{-0.21}$
$\sigma_{\rm jit}$ (m s^{-1})	Uncorrelated jitter	$8.80^{+1.93}_{-1.62}$
γ (m s^{-1})	RV offset	$-18\,733.56^{+2.45}_{-2.33}$

[a]Radius and semimajor axis are derived using our estimate for the stellar radius, $R_* = 0.961^{+0.016}_{-0.015}$ $R_\odot$, and the ratios $R_{\rm p}/R_*$ and a/R_*, respectively.

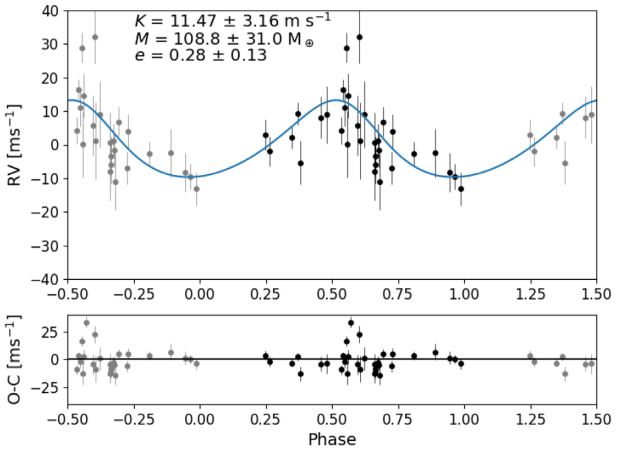

Figure 5. Phase-folded orbital solution (top) and RV residual (bottom) for PH-2b.

The value of uncorrelated jitter in the final model fit is higher than one would expect for a slowly rotating, solar-type star (Collier Cameron et al. 2019). This seems likely due to a combination of some level of stellar activity and high levels of white noise caused by the irregular sampling of the planet's orbit. However, due to the quality of the data, we are unable to place any further constraints on the origin of this additional variability.

To test the viability of the model with such a high jitter, we also modelled the RV data without including a jitter term. The resulting RV semi-amplitude, $K = 13 \pm 1.3$ m s^{-1}, is consistent with the reported result. While it is additionally more precise, we considered the Bayesian information criterion (BIC) of both models when determining which model to present. The BIC of the model including a jitter term is significantly lower than that which did not include jitter, with $\rm BIC_{jitter} = 247.93$, compared to $\rm BIC_{no\text{-}jitter} = 295.17$. As the difference between these two values is significantly larger than 10, it can be considered strong evidence that the model including a jitter term is favoured.

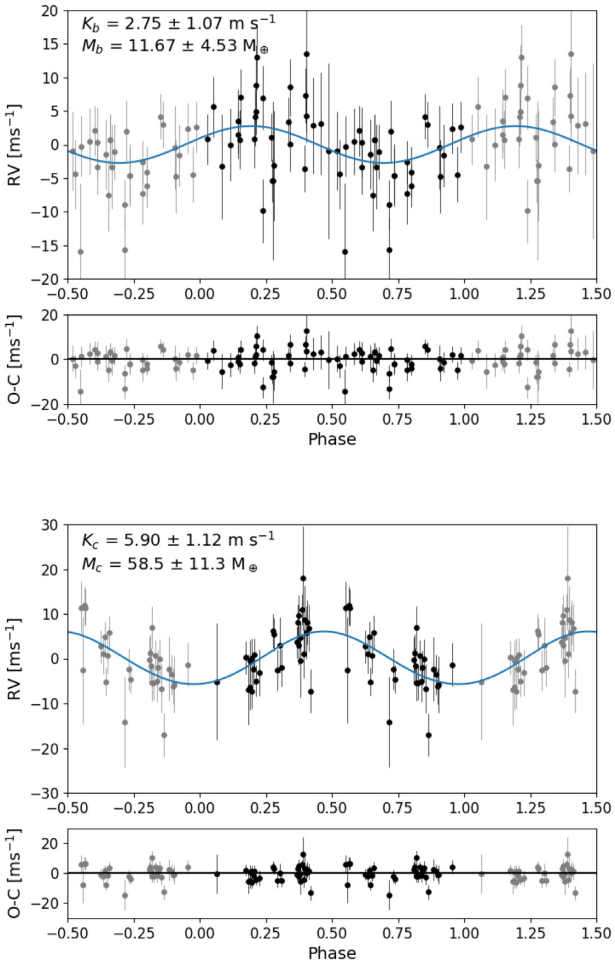

Figure 6. Orbital solutions and RV residuals for Kepler-103b (top) and Kepler-103c (bottom). These are both phase folded on the period of the corresponding planet, and the RV contribution from the other planet has been removed.

Combining the mass estimate with the EXOFAST-determined radius of $R_{\rm p} = 9.49 \pm 0.16$ $R_\oplus$ leads to a density of $\rho_{\rm p} = 0.70^{+0.20}_{-0.21}$ g cm^{-3} $= 0.13 \pm 0.04$ $\rho_\oplus$. This means that PH-2b has a mass and bulk density very similar to that of Saturn. Using the median values, PH-2b has a mass of 1.14 Saturn masses and a density 1.03 times that of Saturn. This strongly suggests that PH-2b is a Saturn-like gas giant.

We also calculated the equilibrium temperature for PH-2b. We used the albedo of Saturn, $A_{\rm Sat} = 0.34$ (page 61, Irwin 2003) and a value of $f = 1$, which is used for non-tidally locked planets that have uniform equilibrium temperatures across both hemispheres. This is a valid assumption, as the large orbital period of this planet means it is unlikely to be tidally locked. We also used the effective temperature, $T_{\rm eff}$, from FASMA (Table 1) and a/R_* from the transit fit . Using these parameters, we obtained a value of $T_{\rm eq} = 251.87^{+3.772}_{-3.755}$ K.

PH-2 had been observed using RV instruments twice before, using the Keck-HIRES (Vogt et al. 1994) and SOPHIE (Perruchot et al. 2008) spectrographs. The HIRES observations were taken in 2013, and are discussed in Wang et al. (2013). Four RV measurements were obtained, with formal internal uncertainties of $\sigma \approx 2$ m s^{-1}. The RMS of this data is 14.0 m s^{-1}, indicating that the formal uncertainties were likely underestimated, and no constraints

could be placed on properties of the orbiting companion of this star. However, based on statistical considerations of the properties of different types of companions, they did conclude that PH-2b should be a giant planet with a 'very high likelihood'. The SOPHIE data consists of a further four RV points, discussed in Santerne et al. (2015). The RMS of these points is 20.0 m s^{-1}, and they found a correlation ($r = 0.80$) between the RV and the bisector span, which we do not recover in our analysis (see Section 5.1.2). Hence, they concluded that they were also unable to confirm the planetary nature of the candidate. Thus, with the lower errors and RMS of HARPS-N, and by finding a $>3\sigma$ mass value, this is the first work that is able to confidently say that the companion of PH-2 is indeed a planet.

In an attempt to improve the precision of our parameter values, we also included both the SOPHIE and HIRES data in the RV analysis. However, since the errors in both data sets were larger than those from HARPS-N, there was no significant improvement in the precision of the final parameters. As a result, we used only the HARPS-N data in our final analysis.

5.2.2 *Kepler-103*

Two planets are known to be present in the Kepler-103 system, with current mass constraints of $M_b = 9.7 \pm 6.8$ M$_\oplus$ and $M_c = 36.1 \pm 25.2$ M$_\oplus$ (Marcy et al. 2014). Our goal was to use the HARPS-N RVs to reduce these uncertainties, and thus report the first precise mass measurements for these planets.

Table 7 gives the results of both the PYORBIT RV model and the EXOFAST transit model for Kepler-103, and Fig. 6 shows the orbital solution and residuals from the RV analysis. We present the orbital period, semi-major axis, and the quantities derived from the RVs (RV semi-amplitude, planet mass, eccentricity, and density) as well as the uncorrelated jitter and RV offset. The posterior distributions of the derived quantities for Kepler-103b and Kepler-103c are shown in Fig. D2. Most of the parameters are well-constrained distributions, as one would expect for a converged solution. We find tails in both eccentricity distributions. However, the eccentricities for both Kepler-103b and Kepler-103c are also consistent with 0 at 2.45σ, which suggests that the eccentricity results are not significant (Lucy & Sweeney 1971).

From the RV fits, we find a 2σ result for the RV semi-amplitude of Kepler-103b and a 5σ result for Kepler-103c. The derived planet masses are $M_{p,b} = 11.67^{+4.31}_{-4.73}$ M$_\oplus$ and $M_{p,c} = 58.47^{+11.17}_{-11.43}$ M$_\oplus$. These are consistent with, but more precise than, the results presented in Marcy et al. (2014).

Using these mass values and the planetary radii from the transit analysis, we obtain planetary densities of $\rho_b = 1.52^{+0.57}_{-0.61}$ g cm^{-3} $= 0.28 \pm 0.11 \rho_\oplus$ for Kepler-103b and $\rho_c = 1.98^{+0.44}_{-0.42}$ g cm^{-3} $= 0.36 \pm 0.08 \rho_\oplus$ for Kepler-103c. This suggests that Kepler-103b has a Neptune-like bulk density. Kepler-103c, with a mass in between that of Neptune and Saturn, has no Solar system analogue.

For both planets, we again assumed a Saturn-like albedo. Using this, we estimate the equilibrium temperature, T_{eq} of the planets to be $T_{eq,b} = 874.02^{+11.54}_{-11.41}$ K and $T_{eq,c} = 390.10^{+5.13}_{-5.10}$ K, for planets b and c respectively.

Kepler-103 has also been observed previously using the Keck-HIRES spectrograph (Vogt et al. 1994). Marcy et al. (2014) used 19 HiRES radial velocities to produce mass estimates for Kepler-103b and Kepler-103c. We did carry out an analysis that combined the HARPS-N RVs presented here with the 19 HiRES RVs presented in Marcy et al. (2014), but this did not improve the precision of our mass estimates. Hence, we report only on the results obtained using the HARPS-N RVs.

5.2.3 *Including stellar activity*

It is now well-known that including stellar activity in the RV analysis can often improve the accuracy of the resulting mass estimates (see Fischer et al. 2016, for an overview). As discussed in Section 3.3, we carried out a GP analysis on the Kepler light curves for PH-2 and for Kepler-103 and recovered rotation periods consistent with those determined through the ACF analysis.

We also carried out RV analyses in which we included stellar activity and assumed that the quasi-periodic kernel is the best choice to model the stellar activity induced RV variations. We used the parameters determined in Section 3.3 as priors for the stellar activity model.

The results are consistent with those presented in Table 7, but are much less precise. This is either because, as discussed in Section 5.1.2, the stellar activity is not strong enough to significantly influence the RVs in this data set or because the RV sampling is insufficient to constrain this activity. Consequently, since we cannot firmly comment on the activity levels of this star with this data, we present the results we obtained without including stellar activity in the RV analysis.

6 DISCUSSION

6.1 PH-2b

Fig. 7 places PH-2b in the context of the larger sample of known exoplanets.[7] We find that PH-2b fits in well with the other Saturn-like planets, even within the parameter errors. The planet's parameters nicely follow the MR relation for longer-period giant planets from Mordasini et al. (2012). We can also use its equilibrium temperature to infer that this planet is likely not highly irradiated. A large fraction of the well-studied population of hot Jupiters are known to have inflated radii compared to their longer-period counterparts (Demory & Seager 2011; Sestovic, Demory & Queloz 2018). The possibility of this trend also being seen in the Saturn-like population is something that has been less investigated, due to the lack of planets that fall into this category. The NASA Exoplanet Archive[8] lists 24 planets as having masses similar to Saturn (we considered masses in the range of 0.27–0.345 M$_J$ as Saturn-like). Of these, 20 are short-period planets, 19 of which have radii at least 10 per cent larger than Saturn. Of the remaining planets with approximately Saturn masses, only one is comparable to PH-2 in terms of period, Kepler-16b (discussed further below). It is also likely not inflated, possibly supporting the theory that the Saturn population displays the same behaviour as the Jupiters – i.e. the irradiated section of the population is significantly inflated when compared to the rest. Determining whether this is indeed the case is beyond the scope of this paper, as many more long-period Saturn-like planets are needed to properly distinguish between the two populations.

Fig. 8 demonstrates that our knowledge of long-period giant planets is sparse. PH-2b is one of only four planets with periods longer than 200 d that have measured masses and radii. Of these,

[7]Data from http://www.exoplanet.eu; accessed 2019 July 03
[8]https://exoplanetarchive.ipac.caltech.edu/, accessed September 2019

Table 7. Parameter values from the Kepler-103 transit and RV analyses.

Parameter	Description	Kepler-103b	Kepler-103c
Transit analysis			
P (d)	Orbital period	$15.965\,328\,7^{+0.000\,009\,1}_{-0.000\,009\,2}$	$179.609\,78^{+0.000\,19}_{-0.000\,20}$
$T_{\rm cent}$ (BJD)	Mid-transit time	$2\,455\,677.652\,43^{0.000\,28}_{-0.000\,28}$	$2\,455\,667.159\,73^{0.000\,44}_{-0.000\,43}$
$R_{\rm p}/R_*$	Radius ratio	$0.021\,40^{+0.000\,11}_{-0.000\,11}$	$0.033\,51^{+0.0011}_{-0.000\,82}$
$R_{\rm p}$ ($R_\oplus$)[a]	Planet radius	$3.4857^{+0.0567}_{-0.0536}$	$5.4539^{+0.1770}_{-0.1746}$
i (deg)	Inclination	$87.914^{+0.073}_{-0.072}$	$89.704^{+0.12}_{-0.055}$
a/R_*	Scaled semimajor axis	$19.52^{+0.34}_{-0.34}$	98.0 ± 1.7
a (au)[a]	Orbital semimajor axis	$0.1330^{+0.0039}_{-0.0016}$	$0.6679^{+0.0193}_{-0.0082}$
RV analysis			
K (m s^{-1})	RV semi-amplitude	$2.75^{+1.05}_{-1.09}$	$5.90^{+1.11}_{-1.13}$
e	Eccentricity	$0.171^{0.288}_{-0.124}$	$0.103^{+0.092}_{-0.068}$
ω	Argument of pericentre	$-0.815^{+2.301}_{-1.439}$	$-0.272^{+1.467}_{-1.045}$
$M_{\rm p}$ ($M_\oplus$)	Planet mass	$11.67^{+4.31}_{-4.73}$	$58.47^{+11.17}_{-11.43}$
ρ (g cm^{-3})	Planet density	$1.52^{+0.57}_{-0.61}$	$1.98^{+0.44}_{-0.42}$
		Common parameters from RV analysis	
$\sigma_{\rm jit}$ (m s^{-1})	Uncorrelated jitter	$1.93^{+1.03}_{-1.11}$	
γ (m s^{-1})	RV offset	$-28490.371^{+0.679}_{-0.678}$	

[a]Radii and semimajor axes are derived using our estimate for the stellar radius, $R_* = 1.492^{+0.024}_{-0.022}$ $R_\odot$, and the ratios $R_{\rm p}/R_*$ and a/R_*, respectively.

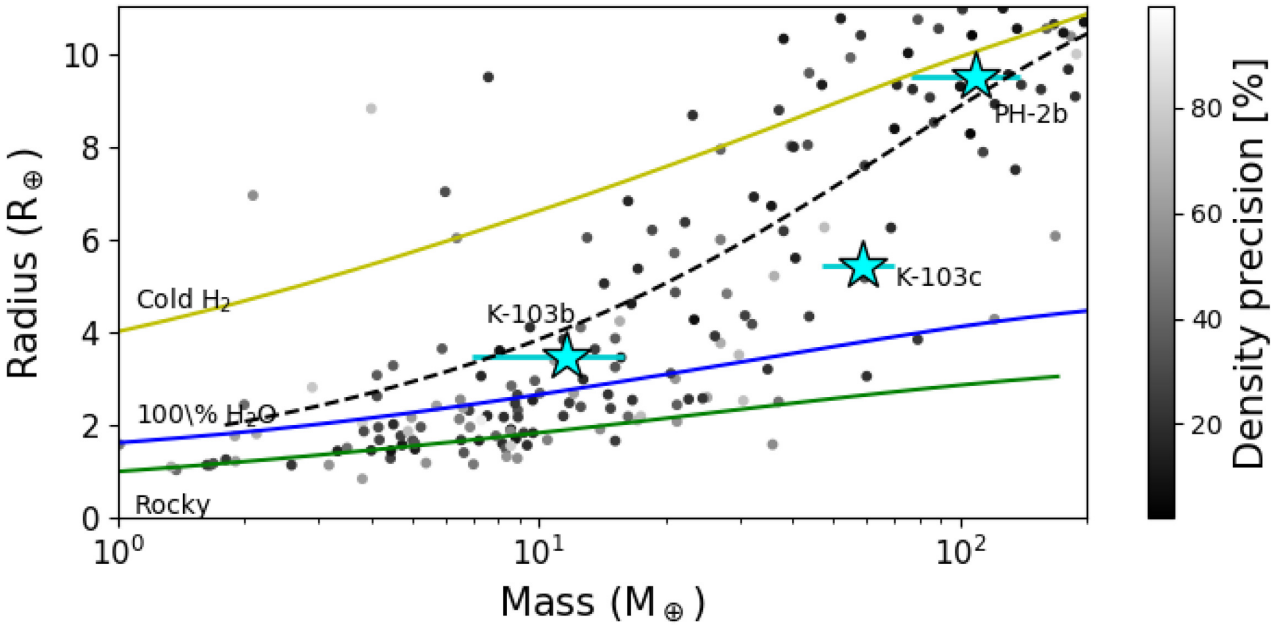

Figure 7. Planet radius versus planet mass for all known exoplanets with a radius smaller than 11 $R_\oplus$ and a mass smaller than 200 $M_\oplus$ (using http://www.exoplanet.eu (Schneider et al. 2011), accessed 2019 July 3). The points are shaded with density precision where the darker points indicate the most precise measurements. PH-2b, Kepler-103b, and Kepler-103c are shown as cyan stars (note the errors for radius are smaller than the symbol). The solid lines represent planetary interior models for different compositions, top to bottom: H_2 assuming a cold isentropic interior (Becker et al. 2014; Zeng, Sasselov & Jacobsen 2016), 100 per cent H_2O assuming 1 mbar surface pressure and 700 K temperature, and Earth-like rocky (Zeng et al. 2019). The dashed line is a fit to a synthetic planet population for planets with $a > 0.1$ au (Mordasini et al. 2012).

two have densities similar to PH-2b: Kepler-34b (Welsh et al. 2012) and Kepler-16b (Doyle et al. 2011). Kepler-16b has an orbital period of 229 d, and a very well-constrained density of $\rho = 1.031 \pm 0.015$ g cm^{-3}. It orbits an eclipsing binary system composed of a K5 main-sequence star ($T_{\rm eff} = 4450$K) and an M-type red dwarf, at a semi-major axis of 0.7 au. The density of Kepler-34b is also well constrained, $\rho = 0.613^{+0.045}_{-0.041}$ g cm^{-3}, and it has a very similar orbital period to PH-2b, $P = 289$ d. While the planet also orbits a binary star system, the binary components of Kepler-34 differ from those of Kepler-16 – two solar-type G stars with effective temperatures of $T_{\rm eff,A} = 5913 \pm 130$ K and $T_{\rm eff,B} = 5867$ K, respectively. Kepler-34b orbits at a semi-major axis of 1.0896 au , significantly more distant from its host stars than PH-2b. Both of these Saturn-like, long-period planets are

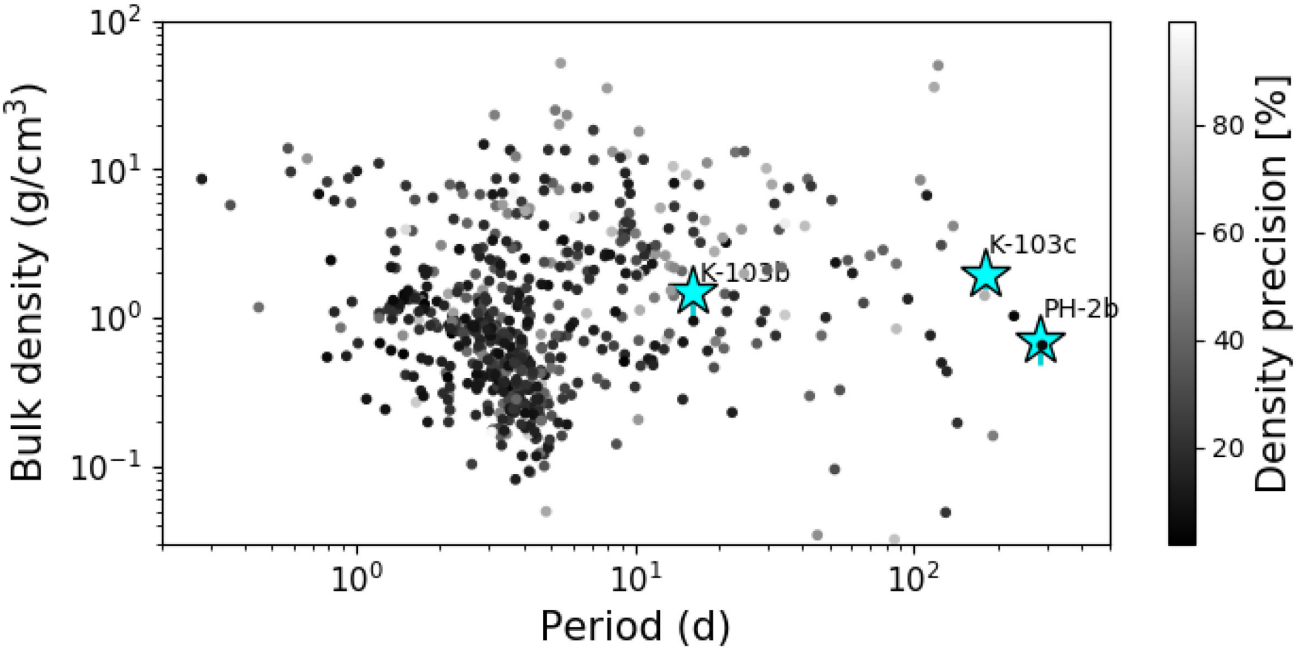

Figure 8. Planetary bulk density versus orbital period for all known exoplanets with measured densities (using http://www.exoplanet.eu (Schneider et al. 2011), accessed 2019 July 03. The points are shaded with density precision where the darker points indicate the most precise measurements. PH-2b, Kepler-103b, and Kepler-103c are shown as cyan stars with errors. Note that most of these errors are smaller than the symbol.

circumbinary. Consequently, PH-2b is the longest-period Saturn-like planet that orbits a single star. If we choose to not use the period to inform our choices of comparison planets, we also find a strikingly similar planet with a period of 95 d. CoRoT-9b, reported by Deeg et al. (2010), also orbits a single star and has a bulk density of 0.9 g cm^{-3}, statistically comparable to PH-2b. Furthermore, it is found to have an equilibrium temperature of 250-430 K. The apparent resemblance of the two objects is another strong indication that the properties of these further-out, less irradiated planets may differ significantly from their closer-in analogues.

The potential habitability of newly discovered objects is often of great interest to the exoplanet community. One way of defining habitability is to consider the spectral type of the star (and thus temperature), and the distance of the planet from the star (semimajor axis, a). Using the methods of Kopparapu et al. (2013) (specifically fig. 7), within the errors on M_* and a, this planet lies just on the edge of the habitable zone for this type of star. There is still much uncertainty as to the most accurate method of defining habitable zones, and we refrain from reaching any concrete conclusions.

Furthermore, considering the habitability of a Saturn-like gas giant would be futile, but this is an interesting result when thinking about potential moons of planets such as this one. Some of the Solar system moons (e.g Enceladus; Waite et al. 2017) are proving to be the most likely places for extraterrestrial life to exist in our Solar system, and so considering this possibility in extra-Solar systems is also interesting. However, the potentially habitable Solar system moons all reside beyond the habitable zone of the Sun, and so the location of exoplanets should not be used to rule conclusively on whether they may have habitable moons.

Recently, Guimarães & Valio (2018) collated a list of the best candidate planets to host a detectable exomoon, using the full *Kepler* database. From 4417 objects that were analysed, they found 54 that were considered the best candidates for detecting the presence of an exomoon using the *Kepler* light curve. PH-2 is among these candidates, identified as a likely candidate for detecting 'icy' moons at a quarter of the maximum possible orbital distance from the planet. Our derived properties not only confirm this candidate as being a planet, but also support this idea of it being a likely exomoon host, due to the similarities of its properties to the Solar system gas giants. Unfortunately, the *TESS* mission (Ricker et al. 2015) will not be able to observe PH-2 (see Christ, Montet & Fabrycky 2019, fig. 1), and so observations of possible exomoons will have to wait for the next generation of transit instruments, such as *PLATO* (Rauer et al. 2014).

6.2 Kepler-103

Fig. 7 also shows the positions of the two planets in the Kepler-103 system in the MR diagram. The planets agree with the general trend seen in MR space. Kepler-103b coincides well with the assumed MR relation from Han et al. (2014), who calculate masses using the MR relations from Weiss & Marcy (2014), Lissauer et al. (2011), and Mordasini et al. (2012). Kepler-103c, on the other hand, lies below the assumed MR relation. However, when the likely intrinsic scatter in the data is considered (Wolfgang et al. 2016), combined with the fact that the MR relations are not very well defined at this time, this discrepancy is probably not significant.

Similarly to PH-2b, Kepler-103c lies in a relatively sparse region of period-density parameter space, as evident in Fig. 8. As of June 2019, there are 14 planets with periods longer than 100 d, with well-constrained densities (i.e. calculated using precise mass and radius measurements).[9] Of these planets, three have densities comparable to Kepler-103c: Kepler-1657b (Hébrard et al. 2019),

[9]https://exoplanetarchive.ipac.caltech.edu/, accessed June 2019

Kepler-539b (Mancini et al. 2016), and HD80606b (Naef et al. 2001; Moutou et al. 2009). These three planets have many parameter values in common: They all have masses similar to, if not multiple times larger than, Jupiter, with Jupiter-like radii, and are at an orbital distance of approximately 0.5 au . In contrast, Kepler-103c is sub-Jupiter in mass and radius and orbits at a distance of $a = 0.66$ au. This suggests it is likely a different kind of object to the other long-period transiting planets characterized so far. Moreover, the properties of these systems can allow us to speculate on possible formation processes for Kepler-103b and c. The high eccentricity ($e = 0.5 \pm 0.03$) of Kepler-1657b has been attributed to planet–planet interactions, after disc dissipation (Hébrard et al. 2019). HD80606b is likely extremely eccentric ($e = 0.934 \pm 0.603$), but as it is in a binary star system this has been attributed to interactions with the outer stellar companion. Both of these systems are examples of formation mechanisms that have left strong detectable traces on the resulting planets, which have likely undergone dynamical orbital evolution. On the other hand, the eccentricities of both Kepler-103b and Kepler-103c are consistent with zero at an $\sim 1\sigma$ level. This suggests a very different evolution history, one that may not involve strong dynamical interactions. Furthermore, these systems are all thought to be of similar ages ($\sim$3.5 Gyr, albeit with extremely large error bars). As a result, it is unlikely that the discrepancy between the properties of these systems can be attributed to each being at different stages in its evolution.

Due to the increased stellar mass and thus effective temperature of Kepler-103, as well as the smaller semimajor axes of the planets in the system, neither Kepler-103b nor Kepler-103c lies in the predicted habitable zone of its host star, again according to the results of Kopparapu et al. (2013).

In Section 4, we presented the TTVs from the Kepler-103 system in Table 4. It was also was previously identified by Holczer et al. (2016) as a system with 'significant long-term TTVs', with the amplitude of the variation found to be $\sim$ 15 min. It is thought that the majority of periodic TTVs are indicative of dynamical interactions with another planet in the system. In this case the possible third planet is likely to be non-transiting, further implied by the discrepancy in inclination (1.774 deg) between the two transiting planets Kepler-103b and Kepler-103c. However, as we only have seven TTV measurements to analyse, it is challenging to obtain a good estimate for the period of this potential third planet, which would be necessary to include it in a further RV fit. We also saw no clear sign of another RV signal in the residuals from the RV fit. As a result, we leave this analysis for a future investigation of this system.

7 CONCLUSIONS

In this work, we have confirmed the existence of a planet in the PH-2 system and presented a 3.5σ mass estimate. We find that PH-2b has a mass of $M_b = 109^{+30}_{-32}\,M_\oplus$ and a radius of $R_b = 9.49 \pm 0.16\,R_\oplus$. This suggests that PH-2b has a similar bulk density to Saturn, with $\rho_b = 1.02^{+0.29}_{-0.31}\,\rho_S$. This is also the first confirmed planet with a Saturn-like mass that has a period of longer than 200 d and that does not orbit a binary star system.

We also recover the first precise mass estimates for the two known planets in the Kepler-103 system. Kepler-103b is found to have a mass of $M_{p,b} = 11.7 \pm 4.5\,M_\oplus$ and a density of $\rho_{p,b} = 1.52^{+0.57}_{-0.61}\,g\,cm^{-3}$, while for Kepler-103c we find $M_{p,c} = 58.5 \pm 11.3\,M_\oplus$ and $\rho_{p,c} = 1.98^{+0.44}_{-0.42}\,g\,cm^{-3}$. This suggests that Kepler-103b has a bulk density similar to Neptune, while Kepler-103c, with a period of $P_c = 179$ d, is one of the densest known long-period exoplanets. It also has no Solar system analogue in terms of density, and so could be a very interesting object to focus further observations on.

These results increase the sample of long-period ($P > 100$ d), intermediate-mass planets with well-constrained mass and radius estimates. This is key in constraining the mass–radius relation across the full range of exoplanet masses and radii, and for gaining a better understanding of the processes involved with planet formation and evolution.

ACKNOWLEDGEMENTS

We would like to thank the anonymous referee for a thorough report that improved the quality of this paper.

The HARPS-N project has been funded by the Prodex Program of the Swiss Space Office (SSO), the Harvard University Origins of Life Initiative (HUOLI), the Scottish Universities Physics Alliance (SUPA), the University of Geneva, the Smithsonian Astrophysical Observatory (SAO), and the Italian National Astrophysical Institute (INAF), the University of St Andrews, Queen's University Belfast, and the University of Edinburgh.

This research has made use of the SIMBAD database, operated at CDS, Strasbourg, France, and NASA's Astrophysics Data System.

Based on observations made with the Italian Telescopio Nazionale Galileo (TNG) operated by the Fundación Galileo Galilei (FGG) of the Istituto Nazionale di Astrofisica (INAF) at the Observatorio del Roque de los Muchachos (La Palma, Canary Islands, Spain).

This paper includes data collected by the *Kepler* mission. Funding for the *Kepler* mission is provided by the NASA Science Mission directorate. Some of the data presented in this paper were obtained from the Mikulski Archive for Space Telescopes (MAST). STScI is operated by the Association of Universities for Research in Astronomy, Inc., under NASA contract NAS5-26555. Support for MAST for non-*HST* data is provided by the NASA Office of Space Science via grant NNX13AC07G and by other grants and contracts.

This work has made use of data from the European Space Agency (ESA) mission *Gaia* (https://www.cosmos.esa.int/gaia), processed by the Gaia Data Processing and Analysis Consortium (DPAC, https://www.cosmos.esa.int/web/gaia/dpac/consortium). Funding for the DPAC has been provided by national institutions, in particular the institutions participating in the Gaia Multilateral Agreement.

This research has made use of the NASA Exoplanet Archive, which is operated by the California Institute of Technology, under contract with the National Aeronautics and Space Administration under the Exoplanet Exploration Program.

AM acknowledges support from Senior Kavli Institute Fellowships at the University of Cambridge. ACC acknowledges support from the Science & Technology Facilities Council (STFC) consolidated grant number ST/R000824/1. AV's and RDH's work was performed under contract with the California Institute of Technology/Jet Propulsion Laboratory funded by NASA through the Sagan Fellowship Program executed by the NASA Exoplanet Science Institute. LM acknowledges support from PLATO ASI-INAF agreement n.2015-019-R.1-2018. This publication was made possible through the support of a grant from the John Templeton Foundation. The opinions expressed in this publication are those of the authors and do not necessarily reflect the views of the John Templeton Foundation. This material is partly based upon work supported by the National Aeronautics and Space Administration under grants No. NNX15AC90G and NNX17AB59G issued through the Exoplanets

Research Program. Some of this work has been carried out in the frame of the National Centre for Competence in Research 'PlanetS' supported by the Swiss National Science Foundation (SNSF).

REFERENCES

Ambikasaran S., Foreman-Mackey D., Greengard L., Hogg D. W., O'Neil M., 2015, IEEE Trans. Pattern Anal. Mach. Intell., 38, 2
Andreasen D. T. et al., 2017, A&A, 600, A69
Angus R., Morton T., Aigrain S., Foreman-Mackey D., Rajpaul V., 2018, MNRAS, 474, 2094
Batalha N. M. et al., 2011, ApJ, 729, 27
Beatty T. G., Gaudi B. S., 2008, ApJ, 686, 1302
Becker A., Lorenzen W., Fortney J. J., Nettelmann N., Schöttler M., Redmer R., 2014, ApJS, 215, 21
Bonfils X. et al., 2011, A&A, 528, A111
Borsato L. et al., 2019, MNRAS, 484, 3233
Borucki W. J. et al., 2010, Science, 327, 977
Charbonneau D., Brown T. M., Latham D. W., Mayor M., 2000, ApJ, 529, L45
Chen J., Kipping D., 2017, ApJ, 834, 17
Christ C. N., Montet B. T., Fabrycky D. C., 2019, AJ, 157, 235
Claret A., Bloemen S., 2011, A&A, 529, A75
Collier Cameron A. et al., 2019, MNRAS, 487, 1082
Cosentino R. et al., 2012, Proc. SPIE Conf. Ser. Vol. 8446, Ground-based and Airborne Instrumentation for Astronomy IV. SPIE, Bellingham, p. 84461V
Cosentino R. et al., 2014, Proc. SPIE Conf. Ser. Vol. 9147, Ground-based and Airborne Instrumentation for Astronomy V. SPIE, Bellingham, p. 91478C
Deeg H. J. et al., 2010, Nature, 464, 384
Demory B.-O., Seager S., 2011, ApJS, 197, 12
Dotter A., 2016, ApJS, 222, 8
Dotter A., Chaboyer B., Jevremović D., Kostov V., Baron E., Ferguson J. W., 2008, ApJS, 178, 89
Doyle L. R. et al., 2011, Science, 333, 1602
Dressing C. D. et al., 2015, ApJ, 800, 135
Eastman J., 2017, Astrophysics Source Code Library, record ascl: 1710.003
Eastman J., Gaudi B. S., Agol E., 2013, PASP, 125, 83
Feroz F., Hobson M. P., 2008, MNRAS, 384, 449
Feroz F., Hobson M. P., Bridges M., 2009, MNRAS, 398, 1601
Feroz F., Hobson M. P., Cameron E., Pettitt A. N., 2013, preprint(arXiv: 1306.2144)
Fischer D. A. et al., 2016, PASP, 128, 066001
Ford E. B. et al., 2011, ApJS, 197, 2
Foreman-Mackey D., 2016, JOSS, 1, 24
Foreman-Mackey D., Hogg D. W., Lang D., Goodman J., 2013, PASP, 125, 306
Fulton B. J. et al., 2017, AJ, 154, 109
Gaia Collaboration et al., 2016, A&A, 595, A2
Gaia Collaboration et al., 2018, A&A, 616, A1
Gaudi B. S., Winn J. N., 2007, ApJ, 655, 550
Giles H. A. C., Collier Cameron A., Haywood R. D., 2017, MNRAS, 472, 1618
Grunblatt S. K., Howard A. W., Haywood R. D., 2015, ApJ, 808, 127
Guimarães A., Valio A., 2018, AJ, 156, 50
Hadden S., Lithwick Y., 2017, AJ, 154, 5
Han E., Wang S. X., Wright J. T., Feng Y. K., Zhao M., Fakhouri O., Brown J. I., Hancock C., 2014, PASP, 126, 827
Haywood R. D. et al., 2014, MNRAS, 443, 2517
Haywood R. D. et al., 2018, AJ, 155, 203
Henden A. A., Levine S., Terrell D., Welch D. L., 2015, American Astronomical Society Meeting Abstracts #225. p. 336.16
Holczer T. et al., 2016, ApJS, 225, 9
Hébrard G. et al., 2019, A&A, 623, A104
Irwin P., 2003, Giant Planets of our Solar System: An Introduction. Springer, Berlin
Kopparapu R. K. et al., 2013, ApJ, 765, 131
Lissauer J. J. et al., 2011, ApJS, 197, 8
Lopez E. D., Fortney J. J., 2014, ApJ, 792, 1
Lucy L. B., Sweeney M. A., 1971, AJ, 76, 544
López-Morales M. et al., 2016, AJ, 152, 204
Malavolta L., Lovis C., Pepe F., Sneden C., Udry S., 2017, MNRAS, 469, 3965
Malavolta L. et al., 2016, A&A, 588, A118
Malavolta L. et al., 2018, AJ, 155, 107
Mancini L. et al., 2016, A&A, 590, A112
Marcy G. W. et al., 2014, ApJS, 210, 20
Mayo A. W. et al., 2018, AJ, 155, 136
Mayor M. et al., 2003, The Messenger, 114, 20
Mordasini C., Alibert Y., Georgy C., Dittkrist K.-M., Klahr H., Henning T., 2012, A&A, 547, A112
Mortier A., Faria J. P., Correia C. M., Santos N. C., 2015, A&A, 573, A101
Mortier A., Sousa S. G., Adibekyan V. Z., Brandão I. M., Santos N. C., 2014, A&A, 572, A95
Mortier A. et al., 2018, MNRAS, 481, 1839
Morton T. D., 2015, Astrophysics Source Code Library, record ascl: 1503.010
Moutou C. et al., 2009, A&A, 498, L5
Naef D. et al., 2001, A&A, 375, L27
Ning B., Wolfgang A., Ghosh S., 2018, ApJ, 869, 5
Noyes R. W., Weiss N. O., Vaughan A. H., 1984, ApJ, 287, 769
Owen J. E., Wu Y., 2013, ApJ, 775, 105
Pepe F., Mayor M., Galland F., Naef D., Queloz D., Santos N. C., Udry S., Burnet M., 2002, A&A, 388, 632
Perruchot S., Kohler D., Bouchy F. et al., 2008, in McLean I. S., Casali M. M., eds, Proc. SPIE Conf. Ser. Vol. 7014, Ground-based and Airborne Instrumentation for Astronomy II. SPIE, Bellingham, p. 70140J
Petigura E. A. et al., 2017, AJ, 154, 107
Rauer H. et al., 2014, Exp. Astron., 38, 249
Rice K. et al., 2019, MNRAS, 484, 3731
Ricker G. R. et al., 2015, JATIS, 1, 014003
Rogers L. A., 2015, ApJ, 801, 41
Santerne A. et al., 2015, MNRAS, 451, 2337
Schneider J, Dedieu C, Le Sidaner P, Savalle R, Zolotukhin I, 2011, AA&A, 532, 11
Seager S., Kuchner M., Hier-Majumder C. A., Militzer B., 2007, ApJ, 669, 1279
Sestovic M., Demory B.-O., Queloz D., 2018, A&A, 616, A76
Skrutskie M. F. et al., 2006, AJ, 131, 1163
Smith J. C. et al., 2012, PASP, 124, 1000
Sneden C., 1973, ApJ, 184, 839
Sousa S. G., Santos N. C., Adibekyan V., Delgado-Mena E., Israelian G., 2015, A&A, 577, A67
Sousa S. G., Santos N. C., Israelian G., Lovis C., Mayor M., Silva P. B., Udry S., 2011, A&A, 526, A99
Storn R., Price K., 1997, JOGO , 11, 341
Stumpe M. C., Smith J. C., Catanzarite J. H., Van Cleve J. E., Jenkins J. M., Twicken J. D., Girouard F. R., 2014, PASP, 126, 100
Stumpe M. C. et al., 2012, PASP, 124, 985
Torres G., Andersen J., Giménez A., 2010, A&AR, 18, 67
Van Eylen V., Agentoft C., Lundkvist M. S., Kjeldsen H., Owen J. E., Fulton B. J., Petigura E., Snellen I., 2018, MNRAS, 479, 4786
Vogt S. S., Butler R. P., Rivera E. J., Haghighipour N., Henry G. W., Williamson M. H., 2010, ApJ, 723, 954
Vogt S. S. et al., 1994, in Crawford D. L., Craine E. R., eds, Proc. SPIE Conf. Ser. Vol. 2198, Instrumentation in Astronomy VIII. SPIE, Bellingham,p. 362
Waite J. H. et al., 2017, Science, 356, 155
Wang J. et al., 2013, ApJ, 776, 10
Weiss L. M., Marcy G. W., 2014, ApJ, 783, L6
Welsh W. F. et al., 2012, Nature, 481, 475
Wolfgang A., Rogers L. A., Ford E. B., 2016, ApJ, 825, 19
Zeng L., Sasselov D. D., Jacobsen S. B., 2016, ApJ, 819, 127
Zeng L. et al., 2019, Proc. Natl. Acad. Sci. USA, 116, 9723

APPENDIX A: FULL KEPLER LIGHT CURVES

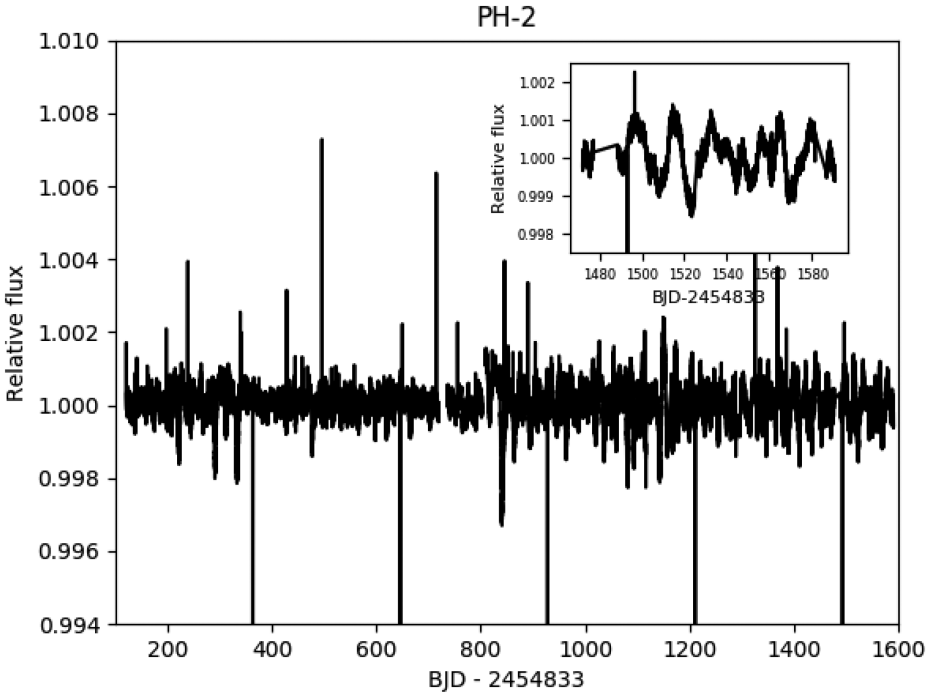

Figure A1. Full *Kepler* light curve, including all quarters in which PH-2 was observed. Inset shows enhancement of the final section of the light curve, to make any variability in the signal easier to identify visually.

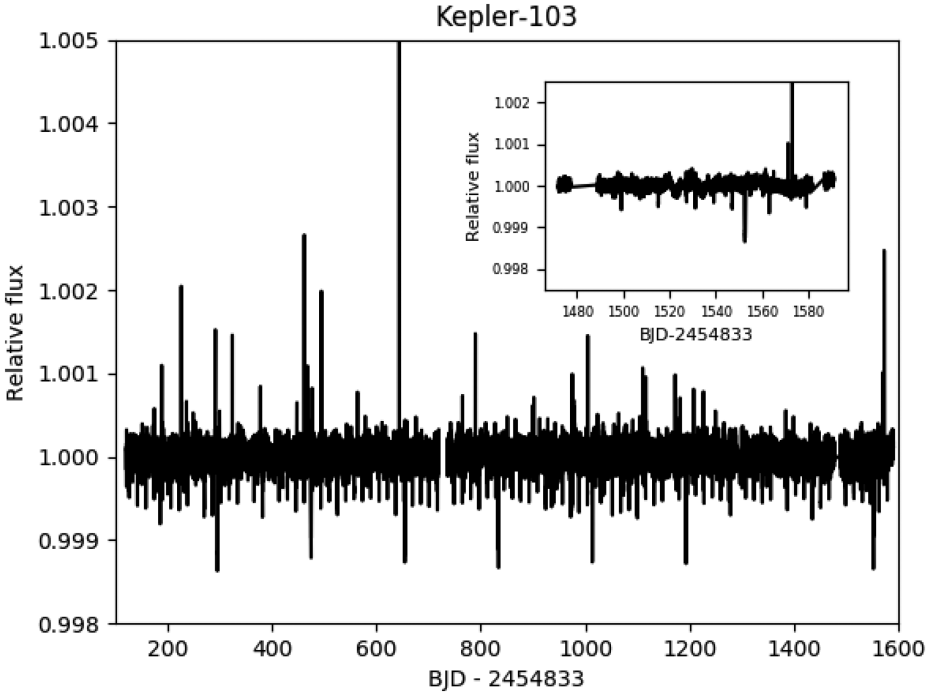

Figure A2. Full *Kepler* light curve, including all quarters in which Kepler-103 was observed. Inset shows enhancement of the final section of the light curve, to make any variability in the signal easier to identify visually.

APPENDIX B: RV DATA FOR PH-2

Table B1. Radial velocity measurements for PH-2, with associated 1σ errors. Also given are the activity indicators; FWHM, contrast, and bisector span.

Time (BJD-2400000)	RV ($km\,s^{-1}$)	Error ($km\,s^{-1}$)	FWHM ($km\,s^{-1}$)	Contrast (%)	Bisector span ($km\,s^{-1}$)	log R'_{HK}
56565.459650	−18.717 10	0.003 05	7.028 21	45.042	−0.017 24	−4.7853
56567.458097	−18.722 63	0.005 39	7.031 70	44.857	−0.018 75	−4.7275
56569.517547	−18.704 65	0.00448	7.037 54	44.920	−0.016 94	−4.8869
56571.481316	−18.719 00	0.006 57	7.064 12	44.631	−0.006 65	−4.6800
56581.411323	−18.727 74	0.008 88	7.022 78	44.066	−0.010 64	−4.6768
56583.363421	−18.701 45	0.007 87	7.024 56	43.151	0.042 52	−4.7448
56604.361465	−18.735 21	0.004 97	7.027 04	44.949	−0.011 46	−4.7726
56608.359816	−18.726 75	0.004 47	7.02449	44.653	−0.026 49	−4.7671
56765.708349	−18.730 62	0.004 51	6.956 05	45.282	−0.026 36	−4.8251
56769.720051	−18.735 57	0.004 54	6.937 00	45.359	−0.018 87	−4.8919
56793.619380	−18.731 42	0.003 36	6.974 80	45.833	−0.016 83	0.0000
56799.707356	−18.724 27	0.003 32	6.936 72	45.522	−0.019 88	−4.8886
56802.652161	−18.738 91	0.006 56	6.957 88	45.418	−0.03348	−4.8140
56824.570925	−18.725 48	0.006 26	6.962 43	48.380	−0.034 17	0.0000
56830.565717	−18.724 64	0.008 53	6.945 60	45.295	−0.015 87	−4.9963
56846.571444	−18.729 34	0.004 12	6.934 62	45.517	−0.014 12	−4.8536
56852.520256	−18.733 40	0.009 81	6.907 91	44.359	−0.013 10	−4.8677
56866.657993	−18.732 43	0.011 49	6.967 97	45.239	−0.012 57	−5.2592
56885.561643	−18.732 47	0.005 01	6.926 26	45.358	−0.037 42	−4.8490
56887.487825	−18.744 67	0.008 44	6.923 45	45.431	−0.024 91	−4.7925
56900.543502	−18.740 56	0.004 82	6.987 39	45.105	−0.030 28	0.0000
56923.454772	−18.736 35	0.003 72	6.940 69	45.508	−0.030 71	−4.8479
56967.395942	−18.743 05	0.003 78	6.93866	45.007	−0.01849	−4.8905
57153.627419	−18.724 50	0.009 96	6.960 27	44.989	−0.04658	−4.7587
57164.712545	−18.741 68	0.008 40	6.967 91	46.070	0.005 01	0.0000
57164.723159	−18.732 98	0.008 92	6.984 20	45.234	−0.039 70	0.0000
57165.700073	−18.73696	0.005 77	6.952 99	45.595	−0.026 10	0.0000
57165.710733	−18.739 48	0.005 70	6.928 62	45.551	−0.010 27	0.0000
57183.698281	−18.729 63	0.005 06	6.916 83	45.609	0.005 62	−4.8693
57229.606372	−18.736 04	0.007 24	6.909 45	45.566	−0.033 78	−5.0336
57256.473584	−18.746 72	0.004 91	6.939 05	45.579	−0.031 14	−4.8579
57527.638124	−18.741 82	0.005 88	6.913 74	45.114	−0.018 15	−4.8576

APPENDIX C: RV DATA FOR KEPLER-103

Table C1. Radial velocity measurements for Kepler-103, with associated 1σ errors. Also given are the activity indicators, FWHM, contrast, and bisector span.

Time (BJD-2400000)	RV ($km\,s^{-1}$)	Error ($km\,s^{-1}$)	FWHM ($km\,s^{-1}$)	Contrast (%)	Bisector span ($km\,s^{-1}$)	$\log R'_{HK}$
56830.522954	−28.499 35	0.00527	8.04057	41.131	0.044 91	0.0000
56831.455893	−28.500 49	0.003 71	8.035 51	41.179	0.019 20	0.0000
56845.651341	−28.486 50	0.003 74	8.050 67	41.116	0.018 17	0.0000
56846.549929	−28.487 71	0.003 72	8.047 96	41.013	0.021 87	0.0000
56848.539131	−28.495 26	0.004 64	8.043 46	40.854	0.021 40	0.0000
56850.502033	−28.488 02	0.00620	8.059 04	40.276	0.034 47	0.0000
56851.543536	−28.491 88	0.004 16	8.01287	40.811	0.022 95	0.0000
56862.546688	−28.484 91	0.003 88	8.04514	41.075	0.025 85	0.0000
56863.509442	−28.483 49	0.004 58	8.02891	41.071	0.030 17	0.0000
56864.515598	−28.487 97	0.003 19	8.05476	41.069	0.018 35	0.0000
56865.557066	−28.481 03	0.003 40	8.030 82	41.134	0.029 61	0.0000
56866.505409	−28.489 89	0.005 46	8.032 30	41.110	0.019 16	0.0000
57186.538255	−28.489 96	0.003 73	8.041 43	41.097	0.018 79	− 5.1056
57188.591209	−28.49526	0.00782	8.058 32	40.919	−0.000 53	− 4.9959
57189.582383	−28.488 29	0.004 68	8.01046	41.084	0.002 50	− 5.2806
57190.595039	−28.48750	0.004 30	8.04686	41.050	0.015 30	− 5.0016
57191.596062	−28.490 29	0.003 58	8.039 95	41.159	0.021 40	− 5.1231
57192.592662	−28.487 81	0.003 66	8.041 05	41.142	0.021 54	− 5.1253
57193.595165	−28.494 52	0.003 47	8.017 04	41.163	0.021 39	− 5.0801
57195.699998	−28.494 94	0.00517	8.038 91	41.005	0.025 16	− 5.1028
57221.484029	−28.484 14	0.003 55	8.023 63	41.136	0.013 15	− 5.1032
57222.458119	−28.484 62	0.004 38	8.018 84	41.115	0.030 77	− 5.0597
57223.642615	−28.488 50	0.008 18	8.049 11	40.999	−0.004 67	− 4.9447
57225.612273	−28.471 64	0.011 67	8.081 35	40.815	0.035 30	− 4.9240
57226.498513	−28.481 95	0.00762	8.046 07	40.936	0.023 69	− 5.0481
57227.474011	−28.485 85	0.005 89	8.038 37	40.968	0.009 90	− 4.9999
57228.500203	−28.484 39	0.004 95	8.065 43	40.942	0.032 84	− 4.9124
57229.498107	−28.486 17	0.005 21	8.047 93	40.983	−0.000 42	− 5.2145
57230.616555	−28.500 34	0.004 81	8.046 98	41.118	0.022 18	− 4.9834
57254.491769	−28.47638	0.005 99	8.028 01	41.193	0.01926	− 5.2237
57255.552280	−28.490 63	0.011 82	8.039 05	40.722	0.00095	− 4.9006
57256.569353	−28.476 88	0.004 22	8.034 08	41.144	0.03198	− 4.9985
57257.504598	−28.478 21	0.004 06	8.043 76	41.128	0.033 18	− 5.1546
57267.529454	−28.486 29	0.003 75	8.029 66	41.050	0.015 04	− 5.0856
57269.488006	−28.486 70	0.004 39	8.033 24	41.109	0.029 57	− 5.2216
57270.475661	−28.482 74	0.003 41	8.050 41	41.101	0.024 51	− 5.0874
57271.478581	−28.493 19	0.003 13	8.035 65	41.115	0.011 32	− 5.1177
57272.517761	−28.487 95	0.004 01	8.045 63	41.088	0.009 02	− 5.0489
57273.494210	−28.483 89	0.003 91	8.010 73	41.152	0.011 64	− 5.0586
57301.455530	−28.486 44	0.004 17	7.998 31	41.120	0.012 74	− 5.0875
57302.456156	−28.480 65	0.004 79	8.033 36	41.095	0.03196	− 5.0952
58361.450610	−28.506 16	0.010 10	8.018 20	40.852	−0.018 78	0.0000
58364.470638	−28.495 44	0.004 62	8.02952	41.060	0.02362	− 5.0950
58365.473987	−28.497 22	0.003 15	8.041 12	41.128	0.01816	− 5.1476
58378.462475	−28.493 12	0.005 22	8.049 47	41.064	0.017 71	− 5.2483
58379.483929	−28.494 72	0.004 06	8.017 45	41.054	0.030 16	− 5.0245
58380.425537	−28.498 43	0.004 09	8.034 22	41.096	0.015 73	− 5.0580
58381.449200	−28.497 99	0.003 84	8.023 95	41.090	0.023 72	− 5.0569
58382.431951	−28.491 10	0.003 42	8.026 84	41.062	0.02315	− 5.0229
58383.432779	−28.495 81	0.004 63	8.045 18	40.902	0.022 56	− 5.0624
58384.432912	−28.491 76	0.003 83	8.02738	41.007	0.002 15	− 5.0250
58385.449051	−28.48885	0.004 54	8.007 77	40.767	0.023 50	− 5.0092
58386.511959	−28.49465	0.005 39	8.002 06	40.318	0.01328	− 4.9821
58388.481621	−28.50472	0.004 76	7.99761	40.893	0.017 47	− 5.0013
58391.497742	−28.492 38	0.007 14	8.039 32	40.814	0.033 80	− 4.9110
58393.444127	−28.495 67	0.004 50	8.035 22	41.206	0.024 14	− 5.0629
58394.427834	−28.498 89	0.004 04	8.033 80	41.195	0.01975	− 5.0829
58395.334495	−28.498 86	0.006 26	8.038 63	40.981	0.022 70	− 5.1372
58404.414404	−28.489 07	0.004 79	8.027 98	41.161	0.01890	− 5.1170
58424.332625	−28.496 22	0.013 05	8.029 04	40.997	0.037 83	− 5.1329

APPENDIX D: CORNER PLOTS FOR THE RV ANALYSES

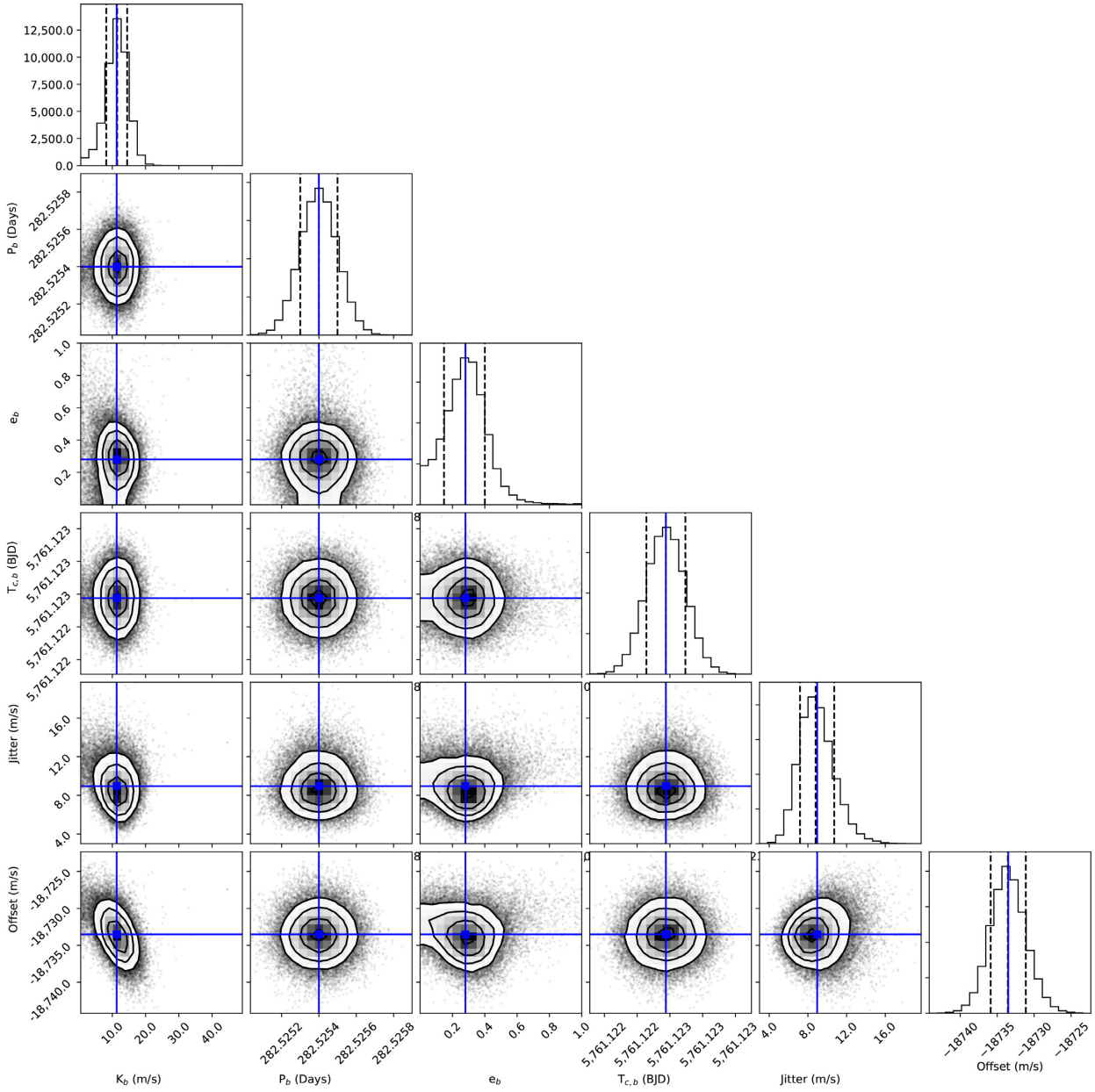

Figure D1. Posterior distributions for the internal variables determined from the PH-2 RV analysis. The contours are at 1, 2, and 3σ. Median values for each parameter denoted by the solid blue lines are those given in Table 6. Made using `corner` (Foreman-Mackey 2016).

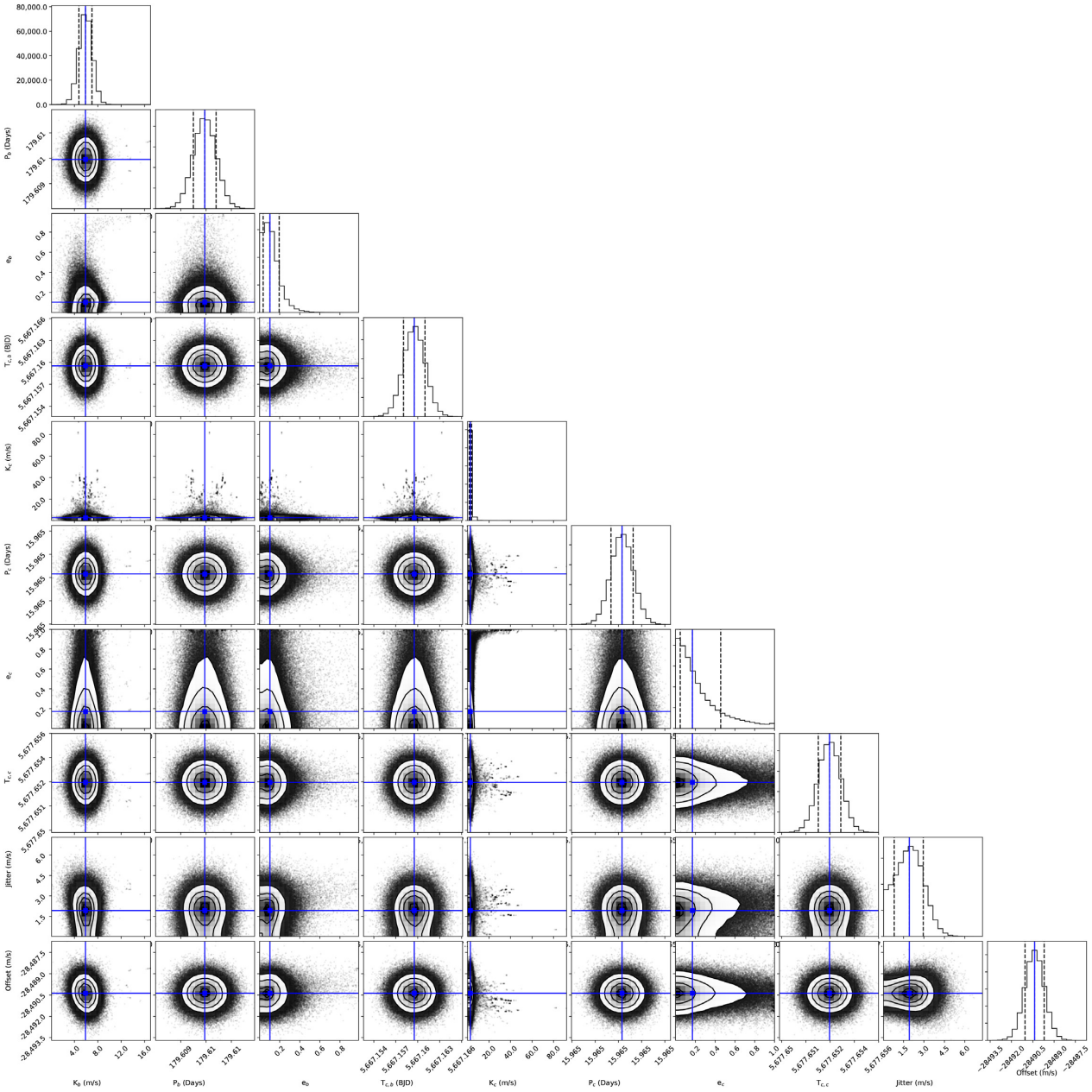

Figure D2. Posteriors distributions for the internal variables determined from the analysis of Kepler-103 RVs. The contours are at 1, 2, and 3σ. Median values for each parameter denoted by the solid blue lines are those given in Table 7. Made using `corner` (Foreman-Mackey 2016).

[1]*SUPA, Institute for Astronomy, Royal Observatory, University of Edinburgh, Blackford Hill, Edinburgh EH9 3HJ, UK*
[2]*School of Physics and Astronomy, University of St Andrews, North Haugh, St Andrews, Fife KY16 9SS*
[3]*Astrophysics Group, Cavendish Laboratory, University of Cambridge, JJ Thomson Avenue, Cambridge CB3 0HE, UK*
[4]*Centre for Exoplanet Science, University of Edinburgh, Edinburgh EH9 3HJ, UK*
[5]*Center for Astrophysics | Harvard & Smithsonian, 60 Garden Street, Cambridge, MA 02138, USA*
[6]*INAF – Osservatorio Astrofisico di Catania, Via S. Sofia 78, I-95123 Catania, Italy*
[7]*Observatoire Astronomique de l'Université de Genève, Chemin des Maillettes 51, CH-1290 Sauverny, Switzerland*
[8]*Department of Astronomy, The University of Texas at Austin, 2515 Speedway, Stop C1400, Austin, TX 78712, USA*
[9]*INAF – Osservatorio Astrofisico di Torino, via Osservatorio 20, I-10025 Pino Torinese, Italy*
[10]*INAF – Fundación Galileo Galilei, Rambla José Ana Fernandez Pérez 7, E-38712 Breña Baja, Tenerife, Spain*
[11]*Instituto de Astrofisica de Canarias (IAC), Calle Vía Láctea s/n, E-38205 La Laguna, Tenerife, Spain*
[12]*Departamento de Astrofisica, Universidad de La Laguna (ULL), E-038206 La Laguna, Tenerife, Spain*
[13]*DTU Space, National Space Institute, Technical University of Denmark, Elektrovej 328, DK-2800 Kongens Lyngby, Denmark*

[14]*INAF – Osservatorio Astronomico di Palermo, Piazza del Parlamento 1, I-90134 Palermo, Italy*
[15]*INAF – Osservatorio Astronomico di Cagliari, via della Scienza 5, I-09047 Selargius, Italy*
[16]*Dip. di Fisica e Astronomia Galileo Galilei, Università di Padova, Vicolo dell'Osservatorio 2, I-35122 Padova, Italy*
[17]*INAF – Osservatorio Astronomico di Brera, Via E. Bianchi 46, I-23807 Merate (LC), Italy*

This paper has been typeset from a TEX/LATEX file prepared by the author.